# Fully Connected Neural Network Model for Fractured Geothermal Reservoir using Supercritical-CO2 as Geofluid with THM Model

# Fully connected neural network model for Fractured Geothermal Reservoir using Supercritical-$CO_2$ as Geofluid with THM Model

Manojkumar Gudala[a,b], Zeeshan Tariq[a,b], Suresh Kumar Govindarajan[e], Zhen Xu[a,b], Bicheng Yan[a,b,*], Shuyu Sun[b,c,d]

[a] *Ali I. Al-Naimi Petroleum Engineering Research Center Physical Science and Engineering (PSE) Division King Abdullah University of Science and Technology (KAUST) Thuwal 23955-6900 Saudi Arabia*
[b] *Energy Resources and Petroleum Engineering Program Physical Science and Engineering (PSE) Division King Abdullah University of Science and Technology (KAUST) Thuwal 23955-6900 Saudi Arabia*
[c] *Computational Transport Phenomena Laboratory (CTPL) Physical Science and Engineering Division (PSE) King Abdullah University of Science and Technology (KAUST) Thuwal 23955-6900 Saudi Arabia*
[d] *Earth Science and Engineering Program Physical Science and Engineering (PSE) Division King Abdullah University of Science and Technology (KAUST) Thuwal 23955-6900 Saudi Arabia*
[e] *Reservoir Simulation Laboratory Petroleum Engineering Programm Department of Ocean Engineering Indian Institute of Technology Madras India-600036*

**Abstract**

In the present work, a thermo-hydro-mechanical (THM) model was utilized to examine the behaviour of fractured geothermal reservoir with supercritical-$CO_2$ ($SCCO_2$) as geofluid. The impact of natural fractures, orientation, and their interaction with hydraulic fractures on the extraction of heat and extension of injection fluid is examined. The development of thermal strain occupied regions were recognized significantly in the vicinity of fracture and injection well. The comparison between water-enhanced geothermal system (EGS) and $SCCO_2$-EGS on the production temperature, thermal strain, and mechanical strain are performed. Injection temperature, injection/production (inj/prod) velocity, aperture of hydraulic fracture (HF), and HF length in a fractured geothermal reservoir are considered as primary control parameters and used as the inputs for the hybrid neural networks and time series models to predict the temperature at the production well. The fully connected neural network (FCN) model shows better predictions based on the loss functions. A mathematical equation is developed using the FCN model to predict the production temperature. Thus, the proposed system of numerical investigations with integrated FCN model could be a benefit in studying the temporal behavior of production temperature.

*Keywords:* Geothermal, $SCCO_2$-EGS, Production temperature, Fully connected neural networks (FCN), Fractures

## 1. Introduction

Geothermal energy is renewable in nature and abundant in the earth's crust. Typically geothermal reservoirs can be categorized into hydro-thermal and hot dry rock (HDR)

*Corresponding author
*Email addresses:* bicheng.yan@kaust.edu.sa (Bicheng Yan), shuyu.sun@kaust.edu.sa (Shuyu Sun)

geothermal reservoirs. HDR geothermal reservoirs have low porosity and permeability, usually available at a depth of $3km$ to 10 km from the surface. As the heat stored in the hot dry rock can not be extracted via conventional engineering techniques, it requires proper selection of injection and production wells connected by hydraulic fractures in high-temperature regions, namely Engineered/Enhanced Geothermal Systems (EGS) [1, 2].

Cold fluid or heat transfer medium (geo-fluid), e.g., water or other working fluid, is injected into EGS to extract the heat energy from the earth's crust to the surface. Recently, $SCCO_2$ has gained much attention as an alternative geo-fluid for heat extraction from geothermal reservoirs. As firstly mentioned by Brown [3], $SCCO_2$ as geo-fluid is superior to water due to its high compressibility, high expansivity, and low viscosity from $SCCO_2$. As a result, there is less resistance for the transport of $SCCO_2$ in the permeable rocks and fractures, which helps reduce the pumping power of injection and so engineering cost. Previous numerical studies in geothermal reservoirs [4, 5, 6, 7, 8, 9, 10, 11, 12, 13, 14, 15, 16, 17, 18] also demonstrated that $SCCO_2$ brings better performance as geo-fluid than water. Besides, the evolution of $CO_2$ plume in reservoirs during geothermal recovery leads to excellent capability of geological $CO_2$ sequestration as well [4, 5, 6, 7, 8, 9].

In EGS, hydraulic and natural fractures influence the heat production and fluid flow. When cold fluid is injected at injection wells, it becomes hotter during the transport process and is ultimately produced as hot fluid at production wells [15, 18, 19, 20, 21, 22, 23]. Natural and hydraulic fractures have better transmissibility than rock matrix and thus act as preferential fluid flow paths [2, 15, 17, 19, 20, 21, 22, 23, 24, 25]. Therefore, the heat recovery from hot dry rocks primarily relies on the distribution of natural and hydraulic fractures [26, 27, 28]. The development of flow field and mechanical forces distribution in the geothermal reservoir mainly depends on the external loads applied and thermal drag [26, 27, 28, 29]. It can generate the stress and strains due to thermal and mechanical variations in the reservoir. Therefore, the geo-fluid type and lateral forces are critical during the heat extraction.

The application of deep learning (DL) models in the energy area rapidly increases with its predictive capability, since DL models can tackle nonlinear high-dimensional problems easily, which is much more efficient than traditional physics-based numerical simulations [30, 31, 32, 33, 34]. DL has been used in the prediction of rock properties, production performance, reservoir fluid properties, well testing applications, geological $CO_2$ sequestration, and production temperature from geothermal reservoirs, to name a few [31, 32, 33, 35, 36, 37, 38, 39, 40, 41, 42, 43, 44, 45, 46, 47, 48]. Recently DNN has also been applied to the prediction of the production temperature at different time nodes in geothermal reservoir modeling [1, 44, 49, 50, 51, 52].

Motivated by these previous works, in this research we focus on the $SCCO_2$ as geo-fluid and also consider the impact of natural fractures in EGS. Firstly, a fully coupled THM simulation model was established to investigate the fractured geothermal reservoir. The dynamic properties of rock, fracture and geo-fluid were considered as the functions of both temperature and pressure. The impact of natural fractures' orientation and their interaction with hydraulic fractures were also evaluated. Further, we develop a hybrid predictive approach, deep neural networks (DNN) and time series models trained from data from the physics simulations were established to predict the production temperature of several proposed scenarios within the maximum and minimum limits of primary control parameters, including

injection temperature, inj/prod velocity, HF aperture, and HF length. The FCN model is developed and utilized to develop a mathematical relation between influencing parameters and production temperature. Response surface methodology (RSM) was utilized to quantify the number of qualitative numerical experiments for the establishment of FCN models.

The manuscript is organized as below. In section 2, we introduce the governing equations of heat transfer, fluid flow, geomechanical for both porous media and fracture. In section 3, we provide the computational model geometry (i.e., section 3.1) and creation of fractures (i.e., section 3.2) in the porous media along with the initial and boundary condition(i.e., section 3.3). The implementation of governing equations and coupled equations is presented section 3.4. In section 4, we provide the results and discussion of temperature variations (i.e., section 4.2) and strain variations (i.e., section 4.3) along with the selection of neural networks for the prediction of the temporal evolution of the production temperature (i.e., section 4.4). Finally, we conclude this work with a few remarks in section 5.

## 2. Mathematical Modeling

### *2.1. Mathematical Equations*

The mathematical formulations relating the transportation of heat and fluid in a rock matrix with geomechanical variations used in the present numerically investigations given in Eq. (1) to Eq. (19). The transfer of heat in the rock matrix is presented in Eq.(1).

$$(\rho C_p)_{eff}\frac{\partial T}{\partial t} + \rho_{fl}C_{p,fl}u_{dlm}\cdot\nabla T - \nabla\cdot(\lambda_{eff}\nabla T) = Q_{matT} + Q_{fracT} \tag{1}$$

$$(\rho C_p)_{eff} = \phi_{mat}\rho_{mat}C_{p,mat} + (1-\phi_{mat})\rho_{fl}C_{p,fl} \tag{2}$$

$$\lambda_{eff} = \phi_{mat}\lambda_{mat} + (1-\phi_{mat})\lambda_{fl} \tag{3}$$

$$u_{dlm} = \frac{\kappa_{mat}}{\mu_{fl}}\nabla p \tag{4}$$

The transfer of heat in the natural/hydraulic fractures is represented in Eq. (5).

$$\begin{aligned}\left(d_{afrc}(\rho C_p)_{eff}\frac{\partial T}{\partial t} + d_{afrc}(\rho_{fl}C_{p,fl})_{frc}u_{frc}\cdot\nabla T - \nabla\cdot(d_{afrc}(\lambda_{eff})_{frc}\nabla T)\right)\\ = d_{afrc}(Q_{matT} + Q_{fracT})\end{aligned} \tag{5}$$

The equation for the flow of geofluid in the natural/hydraulic fractures is given in Eq. (6).

$$d_{afrc}\frac{\partial \phi_{frc}\rho_{fl}}{\partial t} + \nabla_{Tn}\cdot(\rho_{fl}q_{frc}) = d_{afrc}q_m \tag{6}$$

The flow rate ($q_{frc}$) per unit length in the natural/hydraulic fractures is given in Eq. (7).

$$q_{frc} = \frac{-\kappa_{frc}}{\mu_{fl}}d_{afrc}\nabla_{Tn}p_{frc} = \frac{-d_{afrc}^3}{12\mu_{fl}}\nabla_{Tn}p_{frc} \tag{7}$$

Cubic law is employed for the flow of fluid in natural/hydraulic fractures is presented in Eq. (8).

$$u_{frc} = \frac{-d_{afrc}^2}{12\mu_{fl}} \nabla_{Tn} p_{frc} \tag{8}$$

The collective mass conservation and momentum equation [53] has been presented in Eq. (9).

$$\frac{(\partial \phi_{mat} \rho_{fl})}{\partial t} + \nabla \cdot (\rho_{fl} u_{dlm}) - q_m = 0 \tag{9}$$

The mathematical equation which can represents the poroelastic storage is given in Eq. (10)

$$\frac{(\partial \phi_{mat} \rho_{fl})}{\partial t} = \frac{\rho_{fl}}{M} \frac{\partial p_m}{\partial t} \tag{10}$$

The Biot's modulus ($M$) and Biot-Willis coefficient ($\alpha_b$ ) are given in Eq. (11) and Eq. (12), respectively [54, 55].

$$\frac{1}{M} = \frac{\phi_{mat}}{K_{fl}} + (\alpha_b - \phi_{mat}) \frac{1 - \phi_{mat}}{K_d} \tag{11}$$

$$\alpha_b = 1 - \frac{K_d}{K_{fl}} \tag{12}$$

A simplified form of combined hydro and mechanical equation is given in Eq. (13).

$$\rho_{fl} \left[ \frac{\phi_{mat}}{K_{fl}} + \left( 1 - \frac{K_d}{K_{fl}} - \phi_{mat} \right) \frac{1 - \phi_{mat}}{K_d} \right] \frac{\partial p_m}{\partial t} - \nabla \cdot (\rho_{fl} u_{dlm}) = \left( 1 - \frac{K_d}{K_{fl}} \right) \frac{\partial \varepsilon_{vol}}{\partial t} \tag{13}$$

The volumetric strain ($\varepsilon_{vol}$) is described in Eq. (14).

$$\varepsilon_{vol} = \varepsilon_{11} + \varepsilon_{22} \tag{14}$$

In Eq. (14), $\varepsilon_{11}$ and $\varepsilon_{22}$ are the displacement vectors ( $\varepsilon_{ab} = 0.5(\frac{\partial u_{da}}{\partial x_b} + \frac{\partial u_{db}}{\partial x_a})$; $u_{da}$ and $u_{db}$ are the displacement vectors in '$a$' and '$b$' directions, respectively). The governing equation for the equilibrium of forces acting on the computational domain is presented in Eq. (15) [56, 57, 58, 59, 60].

$$\nabla \cdot \left[ \sigma_s - \alpha_b p_m - \varepsilon_T \left( \frac{E}{1 - 2\eta} \right) \right] + (\rho_{fl} \phi_{mat} + \rho_{mat}) = 0 \tag{15}$$

The natural and hydraulic fractures in the computational domain are considered as thin elastic layer in the present work. Force per unit area acting on the fracture is represented mathematically as a function of spring constant ($k_A$), damping constant per unit area ( $d_A$) and fracture thickness (or fracture aperture) ($d_{afrc}$ ) is given in the following Eq. (16).

$$F_A = -K_A(u_u - u_d - u_0) - d_A \frac{\partial (u_u - u_d - u_0)}{\partial t} - 0.5 \rho_{mat} d_{afrc} \frac{\partial^2 (u_u + u_d)}{\partial t^2} \tag{16}$$

Spring constant for unit area is given in Eq. (17).

$$k_A = k_n n \otimes n + k_s(I - n \otimes n) \tag{17}$$

The stiffness in the normal direction, and shear stiffness are defined as a function of both elastic modulus and Poisson's ratios of fractures are given in Eq. (18) and Eq. (19), respectively.

$$k_n = \frac{E_{frc}(1-\nu_{frc})}{d_{afrc}(1+\nu_{frc})(1-2\nu_{frc})} \tag{18}$$

$$k_s = \frac{E_{frc}}{2d_{afrc}(1+\nu_{frc})} \tag{19}$$

*2.2. Rock, Fracture and Fluid properties*

The porosity of rock matrix used in the present work depends on the variation of strains generated due mechanical and thermal loads and is given in Eq. (20) [57, 61].

$$\phi_{mat} = \frac{\phi_{ini} + \Delta\varepsilon_{vol} - \Delta\varepsilon_T}{1 + \Delta\varepsilon_{vol}} = \frac{\phi_{ini} + \Delta\varepsilon_{vol} - [\alpha_T(1-\phi_{ini})\Delta T]}{1 + \Delta\varepsilon_{vol}} \tag{20}$$

The elastic modulus of the rock and fractures is a function of porosity variation (i.e., Eq. (20)) and is represented in Eq. (21) [62].

$$\ln\left(\frac{E}{E_i}\right) = -d(\phi_{mat} - \phi_{ini}) \tag{21}$$

The permeability variation of rock matrix and fractures are represented in Eq. (22) and Eq. (23), respectively [63, 64, 65].

$$\ln\left(\frac{\kappa}{\kappa_0}\right) = [\frac{(1-\phi_{ini})a_1 + b_1\phi_{ini}}{\phi_{ini}}]\varepsilon_{vol} = C_n\varepsilon_{vol} \tag{22}$$

$$\kappa_{frcN} = \kappa_{frc0}\exp\left(\frac{-\sigma_n}{\sigma^*}\right) \tag{23}$$

The rock/fracture heat capacity, thermal conductivity are given in Eq. (24), and Eq. (25) respectively [44, 57].

$$\begin{aligned} C_{p,mat}(\kappa) &= \left[\frac{(2.6log(\kappa)+4.2)\times 10^3}{2.7log(\kappa)+0.3}; if -20 \le log(\kappa) \le -11\right] \\ C_{p,mat}(\kappa) &= [-13log(\kappa)+699; if -11 \le log(\kappa) \le -2] \end{aligned} \tag{24}$$

$$\lambda_r(T) = 2.6 - 0.0025(T - 293.15) \tag{25}$$

The effect of temperature variation on water viscosity, water density, water specific heat and water thermal conductivity are expressed in the mathematical equations and presented in Eq. (26), (27), (28) and (29), respectively [63, 66].

$$\begin{aligned}\mu_w(T) = (1.38 - 0.028T + 1.36 \times 10^{-4}T^2 - 4.61 \times 10^{-7}T^3 + 8.9 \times 10^{-10}T^4 \\ -9.08 \times 10^{-13}T^5 + 3.84 \times 10^{-16}T^6); if 273.15 \leq T \leq 413.15 \\ \mu_w(T) = (0.004 - 2.11 \times 10^{-5}T + 3.86 \times 10^{-8}T^2 + 2.4 \times 10^{-11}T^3); if 413.15 \leq T \leq 553.15\end{aligned} \tag{26}$$

$$\rho_w(T) = 838.47 + 1.4T - 0.003T^2 + 3.72 \times 10^{-7}T^3 \tag{27}$$

$$C_{pw}(T) = 12010.15 - 80.41T + 0.31T^2 - 5.38 \times 10^{-4}T^3 + 3.62 \times 10^{-7}T^4 \tag{28}$$

$$\lambda_w(T) = -0.869 + 0.009T - 1.58 \times 10^{-5}T^2 + 7.98 \times 10^{-9}T^3 \tag{29}$$

The variation of thermodynamics properties of $SCCO_2$ such as viscosity, density, heat capacity and thermal conductivity are given in Eq. (30) to Eq. (33). These properties depend on the temperature and pressure. These equations will be applicable for a temperature range between 273 K to 553 K and pressure range between 15 MPa to 40 MPa [15].

$$\begin{aligned}\mu_{SCCO_2}(T,p) = 7.14 \times 10^{-9}T^2 + 5.642 \times 10^{-6}T - 5.71 \times 10^{-9}p^2 \\ +2.186 \times 10^{-6}p + 0.0011\end{aligned} \tag{30}$$

$$\rho_{SCCO_2}(T,p) = 0.00036T^3 - 0.3693T^2 + 122T - 0.333p^2 + 32.54p - 12720 \tag{31}$$

$$\begin{aligned}C_{p,SCCO_2}(T,p) = -4.9 \times 10^{-5}T^3 + 0.084T^2 - 49.11T \\ -0.47p^3 - 42.1p^2 + 1200p + 276.3\end{aligned} \tag{32}$$

$$\begin{aligned}\lambda_{SCCO_2}(T,p) = -1.75 \times 10^{-8}T^3 + 2.29 \times 10^{-5}T^2 - 0.01T \\ -1.89 \times 10^{-5}p^3 + 0.0007p^2 - 0.006p + 1.46\end{aligned} \tag{33}$$

## 3. Geological model for the Heat Extraction from Geothermal reservoir

### *3.1. Computational Model*

In this work, we used a two-dimensional synthetic porous media geometry of 500 m by 500 m size (and thickness of 30 m) with a hydraulic fracture of length 200 m as depicted in Figure 1. Cold fluid Injection and heat production wells were placed at the extremes of the hydraulic fracture. Hydraulic fracture is the main flow path for the geofluid to gain heat from the surrounding rock. The computational porous domain is having an initial rock porosity of 0.04 and initial rock permeability of $3.2 \times 10^{-16}$ m$^2$ . The natural fractures of length ranging from 5 m to 40 m are considered in the present work with an orientation ranging from 0° to 165° and depicted in Figure 1. Figure 2b depicts the complex reservoir geometry different

arrangements of the natural fractures. The generation of natural fractures were presented in the section 3.2 in detail.

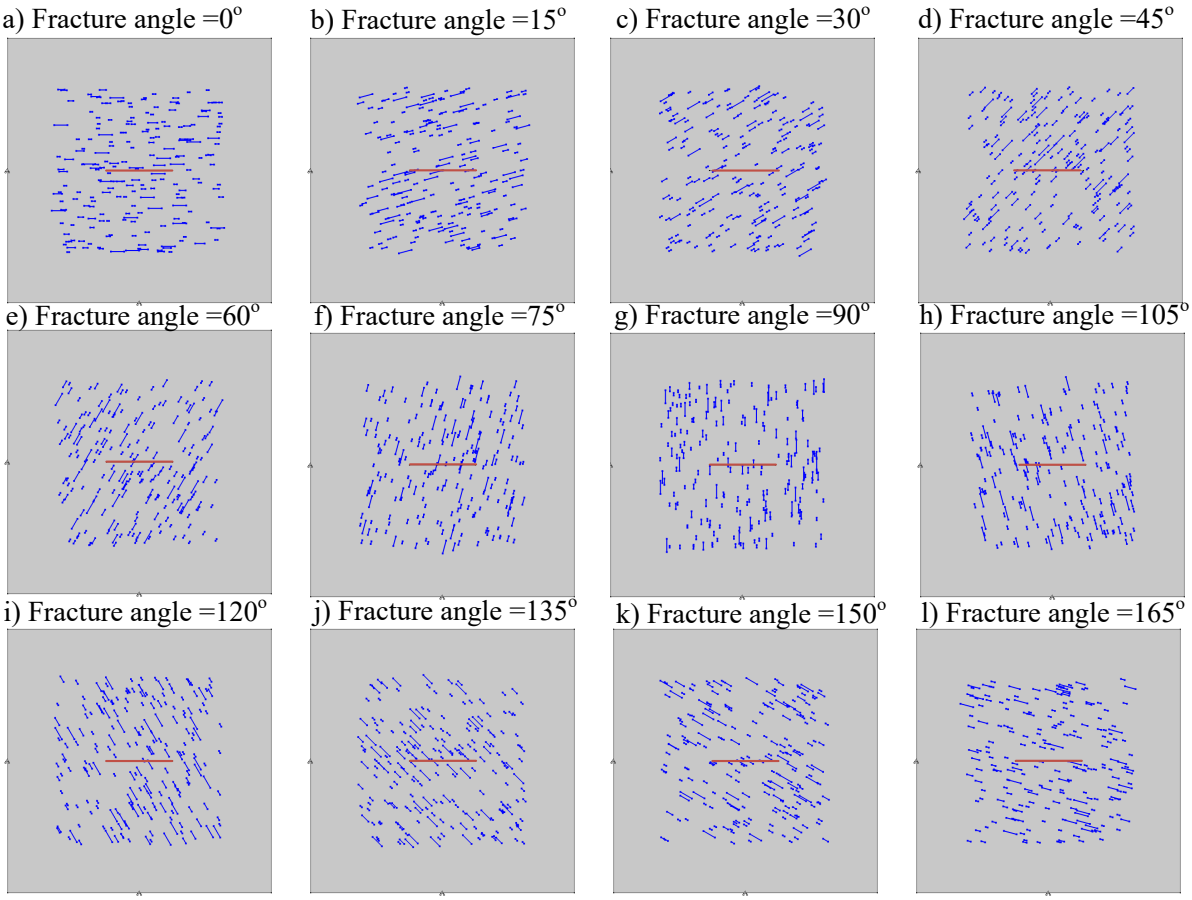


Figure 1: Arrangement of natural fracture in the porous media (Fracture aperture varied from 0.1 mm to 5 mm, and fracture length varied from 1 m to 40 m).

### *3.2. Natural Fracture Geometry*

Development of appropriate fracture network in the porous media is essential to characterize the fluid flow. Espeically in the development of EGS, it will dominate the heat extraction from the rock while geo-fluid moves from injection well to the production well [2, 24, 67]. In the present work power law distribution function was employed to generate the natural fractures in the computational domain. The mathematical representation of the power law distribution is represented in Eq. (34).

$$f(a) = \frac{b-1}{a_{min}} \left( \frac{a}{a_{min}} \right)^{-b} \tag{34}$$

In Eq. (34), $a$ is the population value, $a_{min}$ is the minimum population value, $b$ is the power law exponent. The Fisher distribution is employed to define the orientation of the fracture. The mathematical form of the Fisher distribution is described in the Eq. (35).

$$f(\theta) = K_F \frac{\sin\theta e^{K_F \cos\theta}}{e^{K_F} - e^{-K_F}} \tag{35}$$

In Eq. (35), $K_F$ is the Fisher constant, $\theta$ is the angular deviation of the fracture. Fisher constant ($K_F$ ) indicates the tightness of the of an orientation cluster. The flow characteristics of natural fractures are highly determined by the fracture aperture, orientation and its distribution. In general, the walls of the natural fracture are rough, in the present work we considered that the walls are smooth [68]. The aperture was distributed uniformly between 0.1 mm to 5 mm. The relation between the fracture length and fracture aperture is given in Eq. (36).

$$d_{afrc} = c_{pf} l_{frc} \tag{36}$$

In Eq. (36), $c_{pf}$ is a proportionality factor, $l_{frc}$ is the length of fracture, $d_{afrc}$ is the fracture aperture.

*3.3. Initial and boundary conditions*

The Initial temperature of the geothermal reservoir is considered as 425 K (151.85 °C) with and average reservoir pressure is 15 MPa. The porous domain is appropriate to confine the effects of boundaries throughout the extraction of heat from the rock matrix when operating. So, at the boundaries, the temperatures are constant which is equals to the initial reservoir temperature. At the boundaries of the reservoir no-flow condition was employed for both heat flux and fluid flow. In the geomechanical section two boundaries are considered as rolling and lateral stresses (i.e., $\sigma_x$, and $\sigma_y$) were applied on the other two boundaries (Figure 2*c*). In the Table 1, rock, fracture and injected fluid properties are mentioned. The initial conditions of fluid flow, temperature and displacements field are given in Eq. (37), Eq. (38), Eq. (39), Eq. (40), respectively.

$$p(x, y, t)_{t=0} = p_{ini} \tag{37}$$

$$T(x, y, t)_{t=0} = T_{ini} \tag{38}$$

$$[u_x, u_y]^T_{t=0} = [0, 0]^T \tag{39}$$

$$\left[\frac{\partial u_x}{\partial t}, \frac{\partial u_y}{\partial t}\right]^T_{t=0} = [0, 0]^T \tag{40}$$

The boundary conditions are applied at the production well, injection well and the boundaries of the rock matrix are mainly influencing the changes occur in the reservoir. The fluid flow boundary conditions at the injection well and production well are represented in Eq. (41) and (42), respectively.

$$\text{At injection well} : m(t)_{inj} = u_{inj} \rho_{w/SCCO_2} \tag{41}$$

$$\text{At production well} : m(t)_{prod} = u_{inj} \rho_{w/SCCO_2} \tag{42}$$

Heat flux boundary condition was employed at the injection well and is given in Eq. (43).

$$\text{At injection well} : q(t)_{inj} = C_{p,w/SCCO_2} (T_{inj} - T_0) u_{inj} \rho_{w/SCCO_2} \tag{43}$$

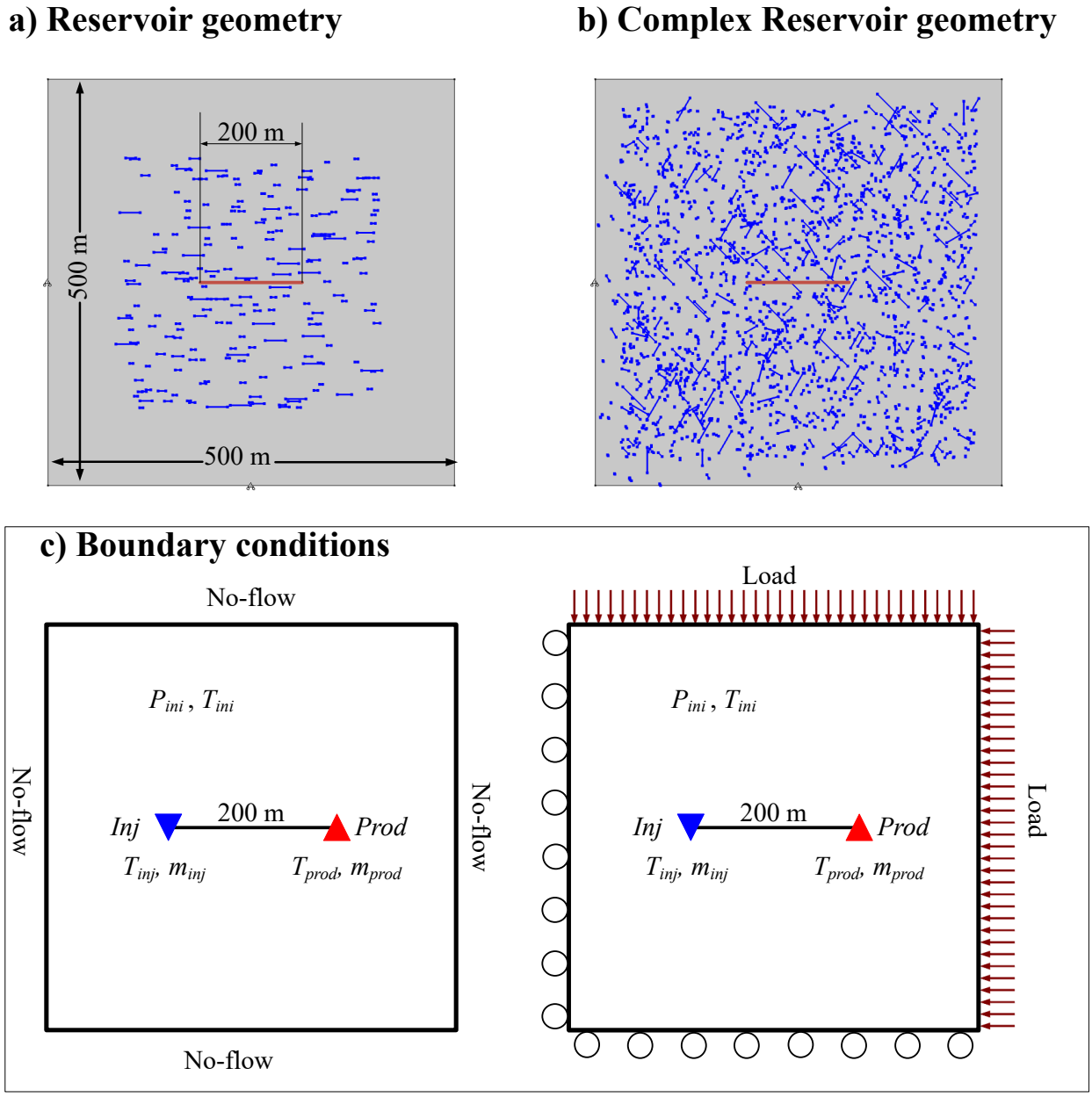


Figure 2: Reservoir geometry and boundary conditions.

*3.4. Implementation in COMSOL Multi-Physics*

COMSOL Multiphysics was utilized in the establishment of fully coupled and dynamic THM model for the geothermal reservoir with natural and hydraulic fractures (Figure 3). Engineers are using COMSOL for employing the fully coupled numerical investigations for geothermal reservoirs [60, 69, 70, 71, 72, 73, 74, 75, 76, 77]. COMSOL Multiphysics integrated with heat transfer, poroelastic, Darcy flow, solid mechanics, thermal expansion modules. These modules will be utilized in the present work and coupled interaction (i.e., Eq. (20) to Eq. (33)) were embedded as local variable in the component section. In the solid-mechanics module, natural and hydraulic fractures are designated as a thin elastic layer, and mathematical formulation is presented from Eq. 16 to Eq. 19. The fluid and heat

Table 1: Rock, fracture and fluid properties

| **Property** | **Rock Properties** | **Fluid Properties** |
|---|---|---|
| Density, kg/m$^3$ | 2600 | Eq. (22) |
| Dynamic viscosity, Pa.s | - | Eq. (21) |
| Thermal conductivity, W/m·K | Eq. (20) | Eq. (24) |
| Heat capacity at constant pressure, J/kg·K | Eq. (19) | Eq. (23) |
| Coefficient of Thermal expansion, K$^{-1}$ | $3 \times 10^{-5}$ | - |
| Initial Youngs Modulus, GPa | 24 | - |
| Poisson's ratio | 0.26 | - |
| Initial Porosity | 0.03 | - |
| Initial Permeability, m$^2$ | $3.2 \times 10^{-16}$ | - |
| Ratio of Specific heats | - | 1.0 |
| Biot-willis coefficient | 0.25 - 0.75 | - |
| Fluid-injection rate, m/s | - | 0.1 |
| Fluid-production rate, m/s | - | 0.1 |
| Initial reservoir Temperature, °C | 180 | - |
| Fluid injection Temperature, °C | - | 20 |
| Initial Youngs Modulus-Fracture, GPa | 2.4 | - |
| Poisson's ratio-Fracture | 0.104 | - |
| Fracture aperture, mm | 0.2 | - |
| Fracture porosity | 1 | - |
| Boundary load: x-direction, MPa | 48 | - |
| Boundary load: y-direction, MPa | 44 | - |

flow in the fractures is employed using the fracture flow physics conditions in both the Darcy's Law and heat transfer modules. Stationary and transient solvers were sequentially employed in the present work. Backward difference formula (BDF) with Euler backward initializing technique was employed. The multifrontal massively parallel sparse (MUMPS) direct linear solver was used for solving pressure and displacement. A parallel direct sparse solver (PARDISO) being used for solving temperature.

## 4. Results and Discussions

### *4.1. Validation*

The fully coupled thermo-hydro-mechanical and its accuracy are validated with single fracture scenario and rock matrix without fracture. The analytical solution (44) given by the Lauwerie's [78] was used to validate the developed model . Fig 4*a* and Fig 4*c* presents the geometry details of validation-1 and validation-2 respectively. The rock and fluid details are taken from the work of Ghassemi and Zhang[79], and Han et al. [80].

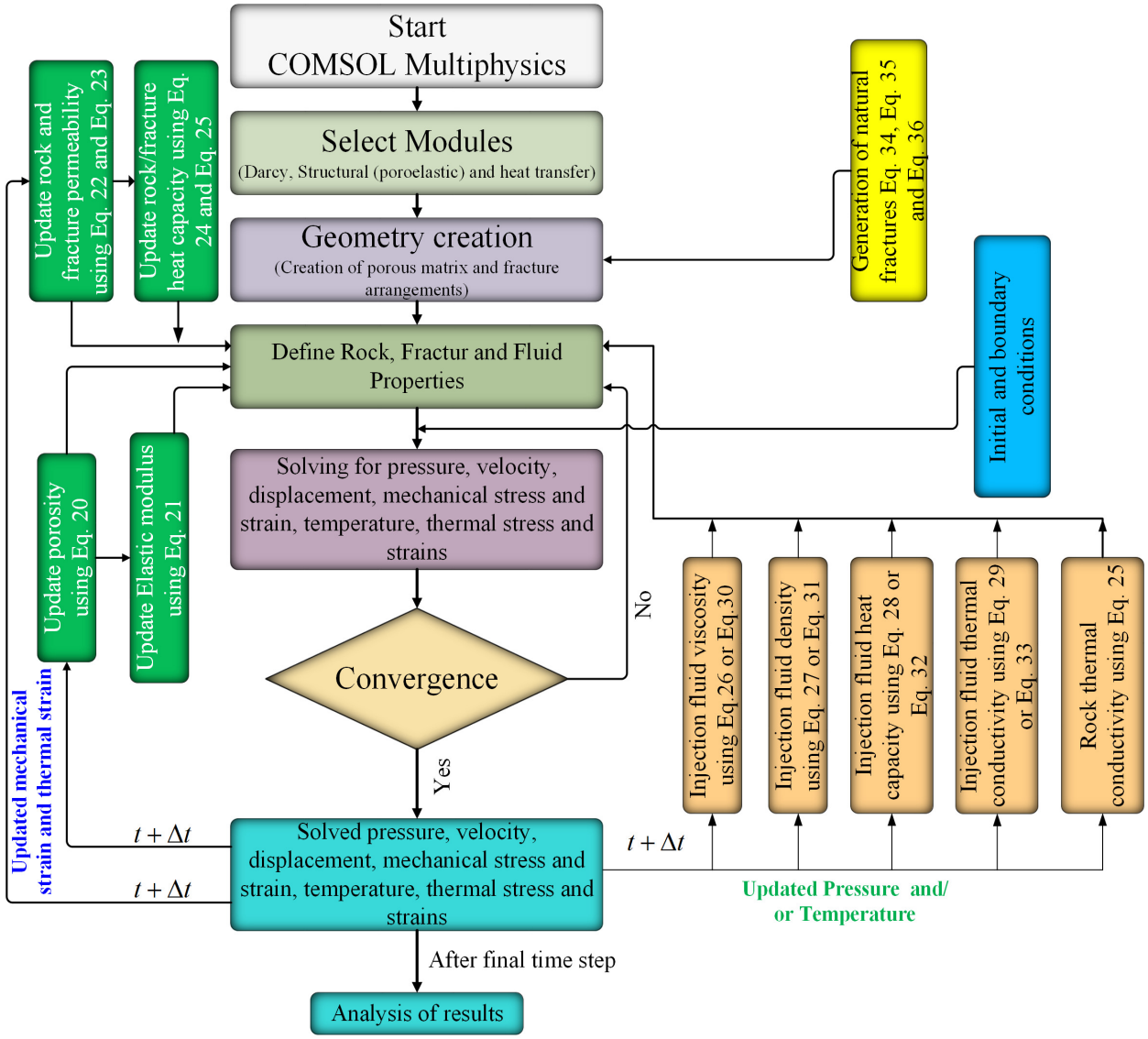


Figure 3: Schematic of the solution process employed for fully coupled Thermo-hydro-mechanical model in present work.

$$T(x,t) = T_0 + (T_{inj} - T_0) erfc \left[ \frac{\lambda_m x}{\rho_w C_{pw} d_f \sqrt{\frac{\lambda_m}{\rho_m C_{pr}} (u_w t - x)}} \right] U\left(t - \frac{x}{u_w}\right) \tag{44}$$

The results from the developed THM model and its comparison with the analytical solution is presented in Figure 4*b* and Figure 4*d* for validation-1 and validation-2, respectively. The comparison of developed THM model results with the analytical solutions provides the greater accuracy. It confirms that the developed THM model is suitable to predict the thermo, hydro, and mechanical variations in the rock matrix and fractures. Thus, the developed model applied to investigate the variations occurs in the fractured geothermal reservoir.

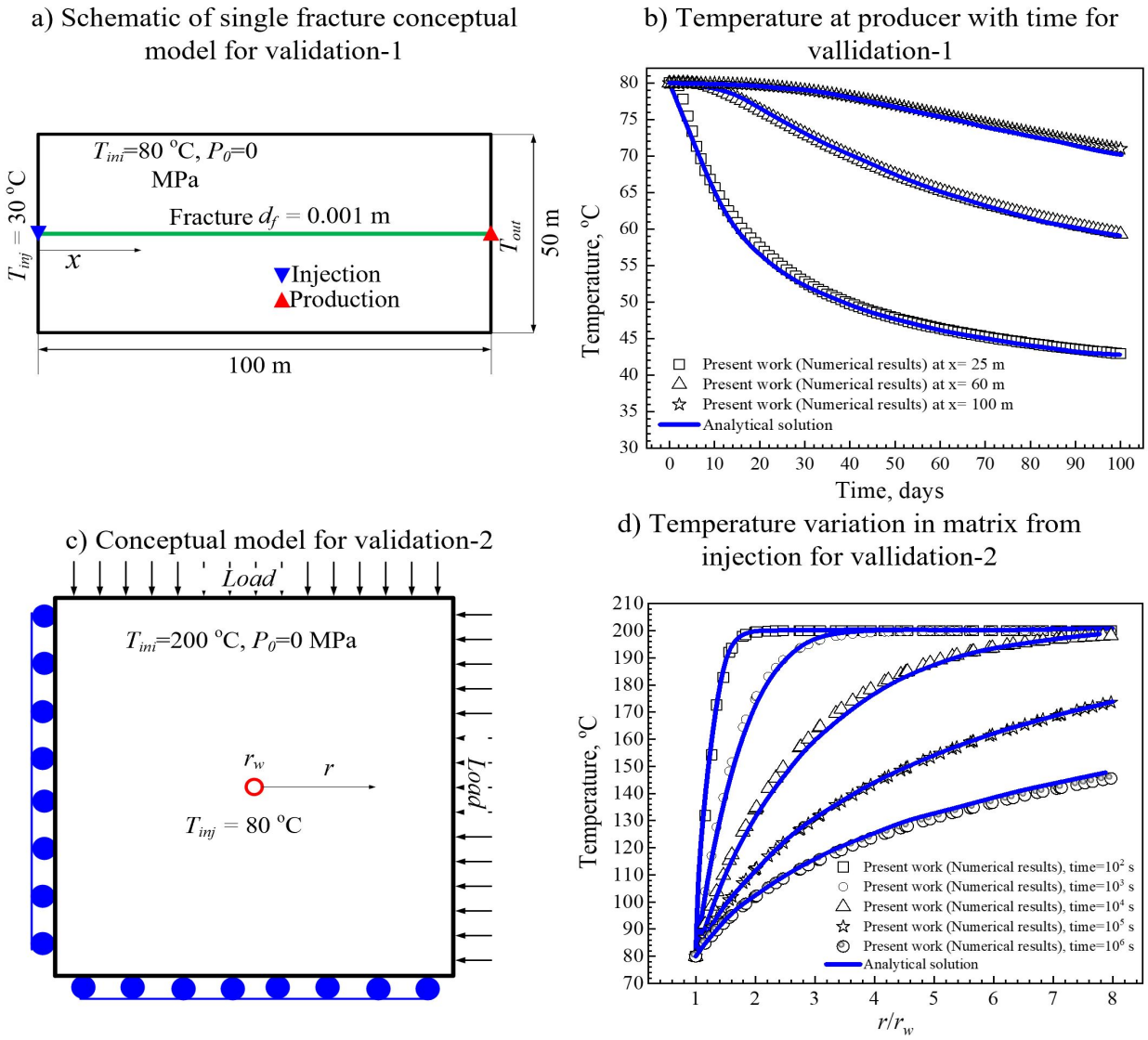


Figure 4: Validation of the developed THM model with single fracture case and only rock matrix case.

### *4.2. Temperature Evolution*

Figure 5 illustrates the spatial and temporal distribution of temperature in the porous media at different arrangement of natural fractures when $SCCO_2$ is used as geofluid. In the early stages, heat transfer transpires among the matrix and the geo-fluid in the hydraulic fracture. Due to the heat conduction between the geo-fluid and rock matrix, the rise in geo-fluid temperature will occur (Figure 5). Concurrently the rock matrix temperature in the neighbourhood of hydraulic fracture decreases, which creates a low temperature region advancing into rock matrix with time. It will reduce the production temperature due to the less extraction of heat compared to the initial stage. It was identified efficiently after five years of the production (Figure 5). The geo-fluid mass and heat exchange are maximum in the locality of the injection well. The influence of natural fractures in the temperature distribution is investigated and presented in Figure 5 and Figure 6. It has been clearly found

that, the injected fluid is moving from the hydraulic fracture to the natural fracture before reaching to the production well (Figure $5b_1 - 5b_4$ and Figure $5c_1 - 5c_4$). It can be seen from the numerical results that the zone adjacent the hydraulic fracture is highly influenced in starting of the heat production (Figure $5a_1 - 5a_4$) and expands via the connected natural fracture in the reservoir (Figure $5b_1 - 5b_4$ and Figure $5c_1 - 5c_4$). Figure 6 depicts the spatial distribution of temperature in the reservoir after 10 years of production. The distribution of low temperature zone is dependent on the orientation of natural fracture and the connectivity of hydraulic fracture with it. Thus, influence of natural fractures in the expansion of low temperature zone is clearly identified from the numerical investigations.

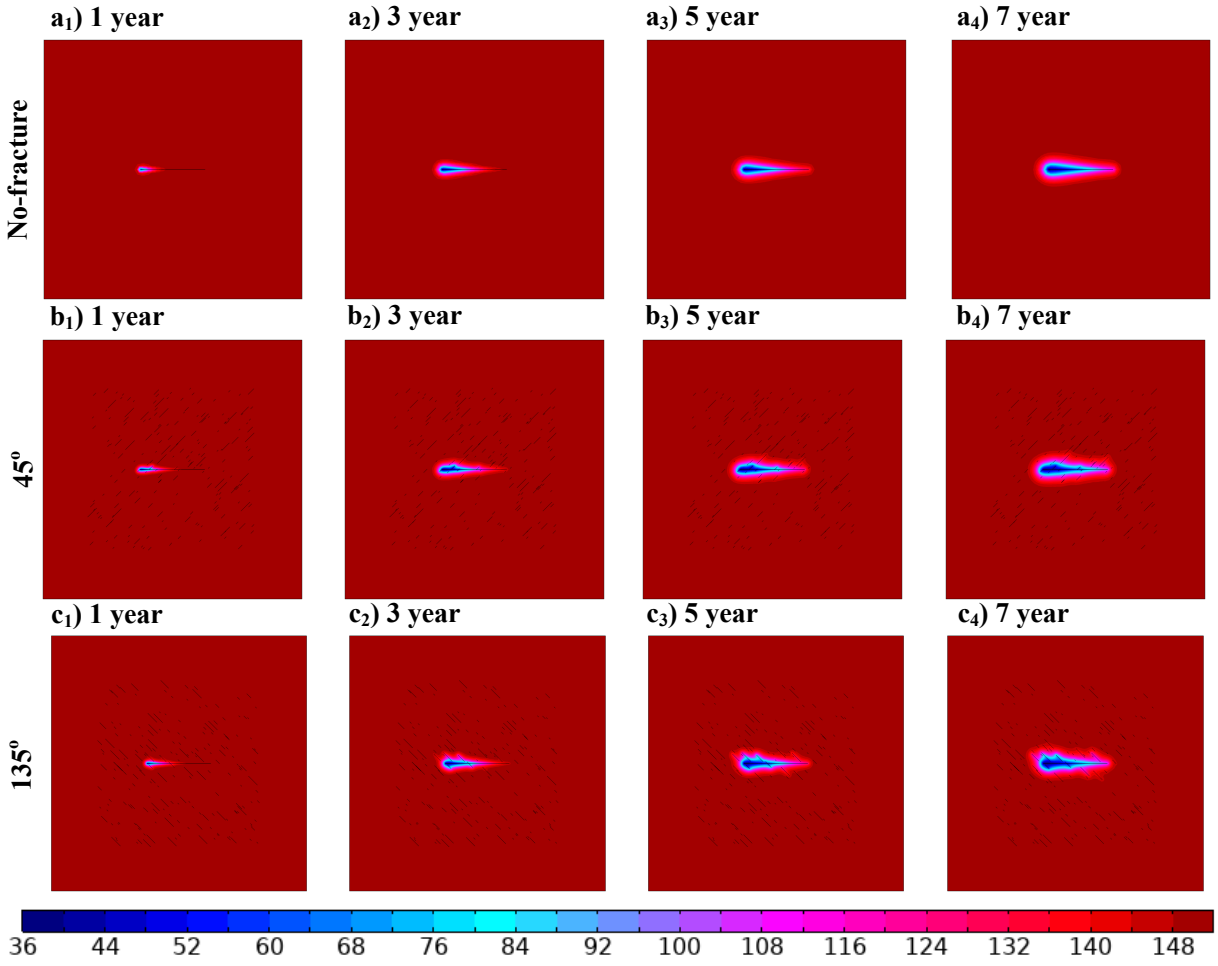


Figure 5: Spatiotemporal variation of temperature in the reservoir at different arrangement of natural fractures while using $SCCO_2$ as geofluid.

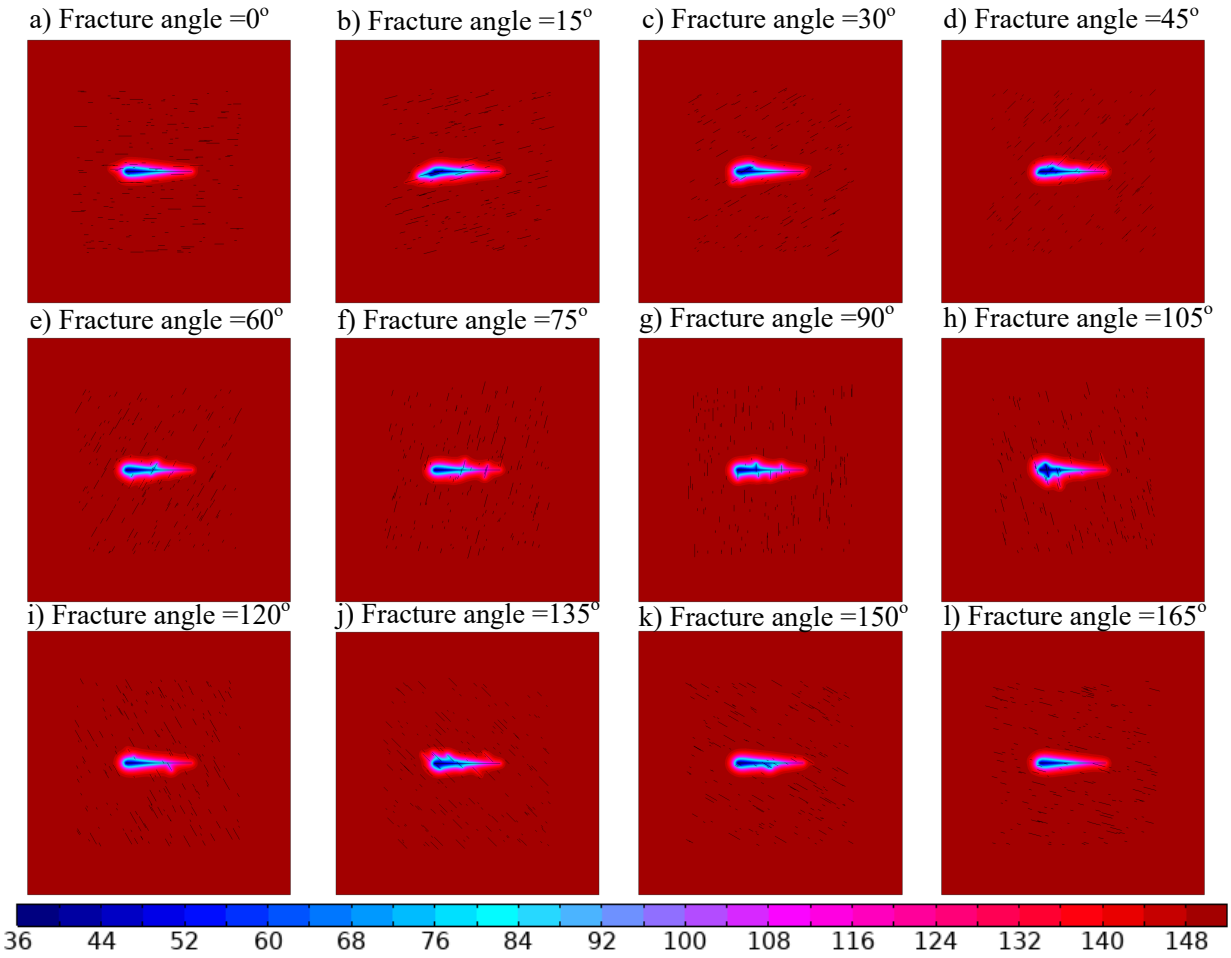


Figure 6: Spatial variation of temperature in the reservoir at different arrangement of natural fractures after 10 years of production.

Figure 7 represents the impact of hydraulic fracture aperture and inj/prod velocity on the temperature at production well. It was also found that the temperature at production well is reduced with an increase in aperture of hydraulic fracture. It will decrease the transfer of heat from matrix to geofluid due to the low residence time before reaching to the production well for small aperture scenario (Figure 7*a*). The temperature at the production well declines with an upsurge in the inj/prod velocity and is illustrated in Figure 7*b*. At higher inj/prod velocity (0.04 m/s) fluid will move faster in the hydraulic fracture and it will reflect in the residence time to be low. Thus, the fluid has a lesser time to transfer heat from the surrounding rock matrix before reaching to the production well. Due to this production temperature will be less compared to the low inj/prod velocity (0.01 m/s to 0.03 m/s). Figure 8 depicts the influence of fracture orientation on the production temperature at same operating conditions. It has been found that the significant impact of production temperature was observed with orientation of natural fracture but not like hydraulic fracture aperture and inj/prod velocity. Thus, the aperture of hydraulic fracture and inj/prod velocity, and orientation of natural fractures influencing the temperature at production well.

Figure 9 depicts the comparison of $SCCO_2$ and water as geofluids on the production temperature at same operating conditions. Sharp decline of production temperature was

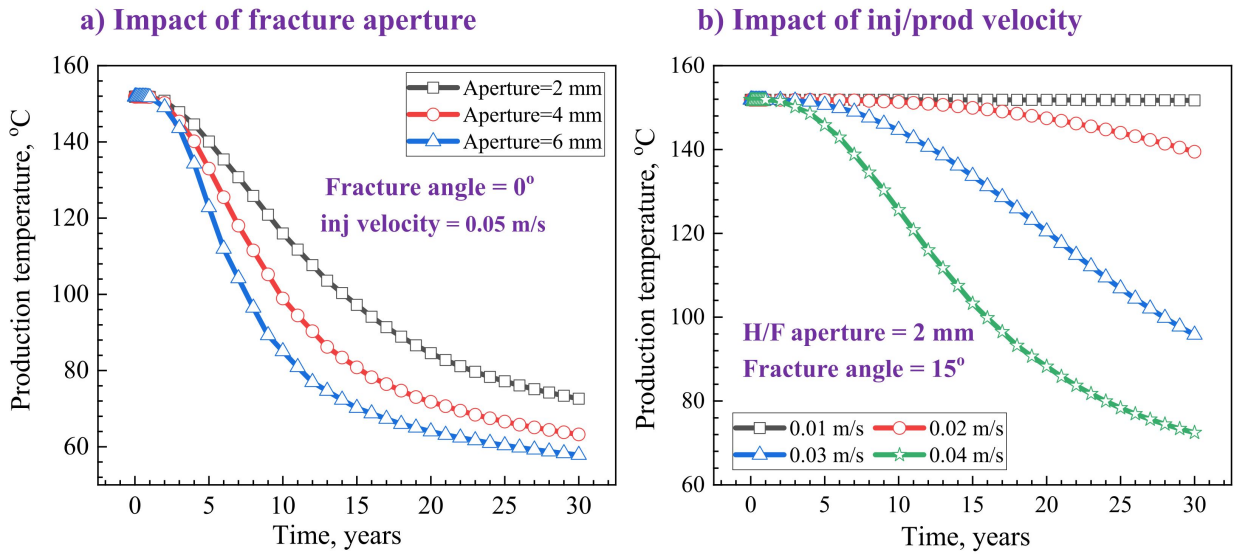


Figure 7: Impact of fracture aperture and injection/production velocity on production temperature.

found when using the water compared to $SCCO_2$ with increase (Figure 9). Aperture of hydraulic fracture is showing negligible influence when water is used as geofluid but $SCCO_2$ is showing significant influence (Figure 9*a*). Injection/production velocity was showing the significant impact on production temperature when using water and $SCCO_2$ as geofluids, but high production temperatures were observed when using $SCCO_2$(Figure 9*b*). Thus, $SCCO_2$ is providing the better production temperature compared to water from the reservoir at same operating conditions.

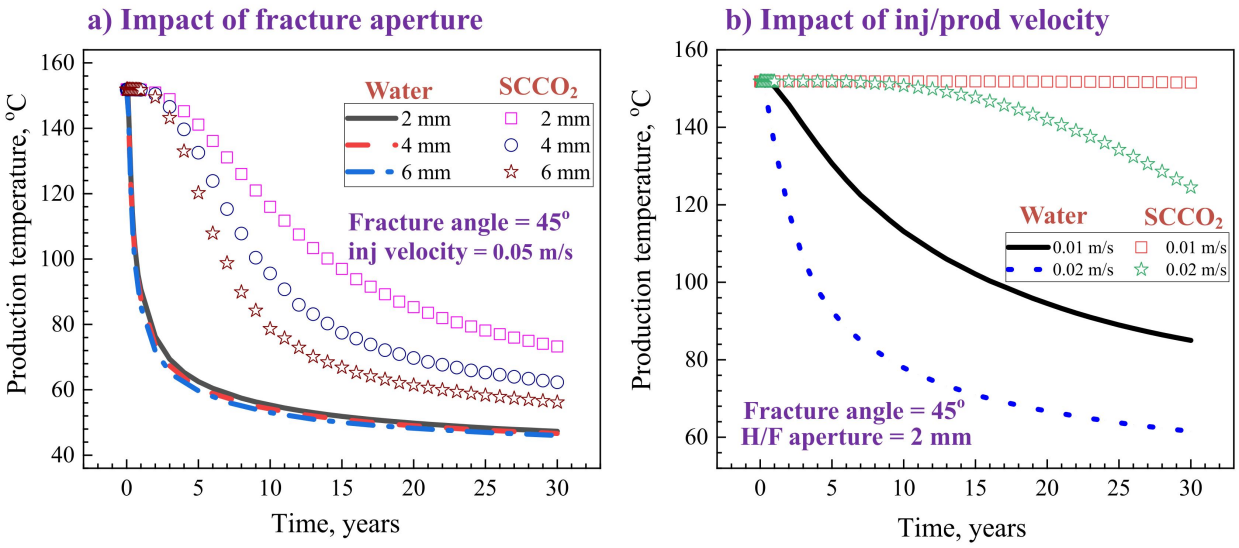


Figure 9: Comparison of $SCCO_2$ and water as geofluids on production temperature.

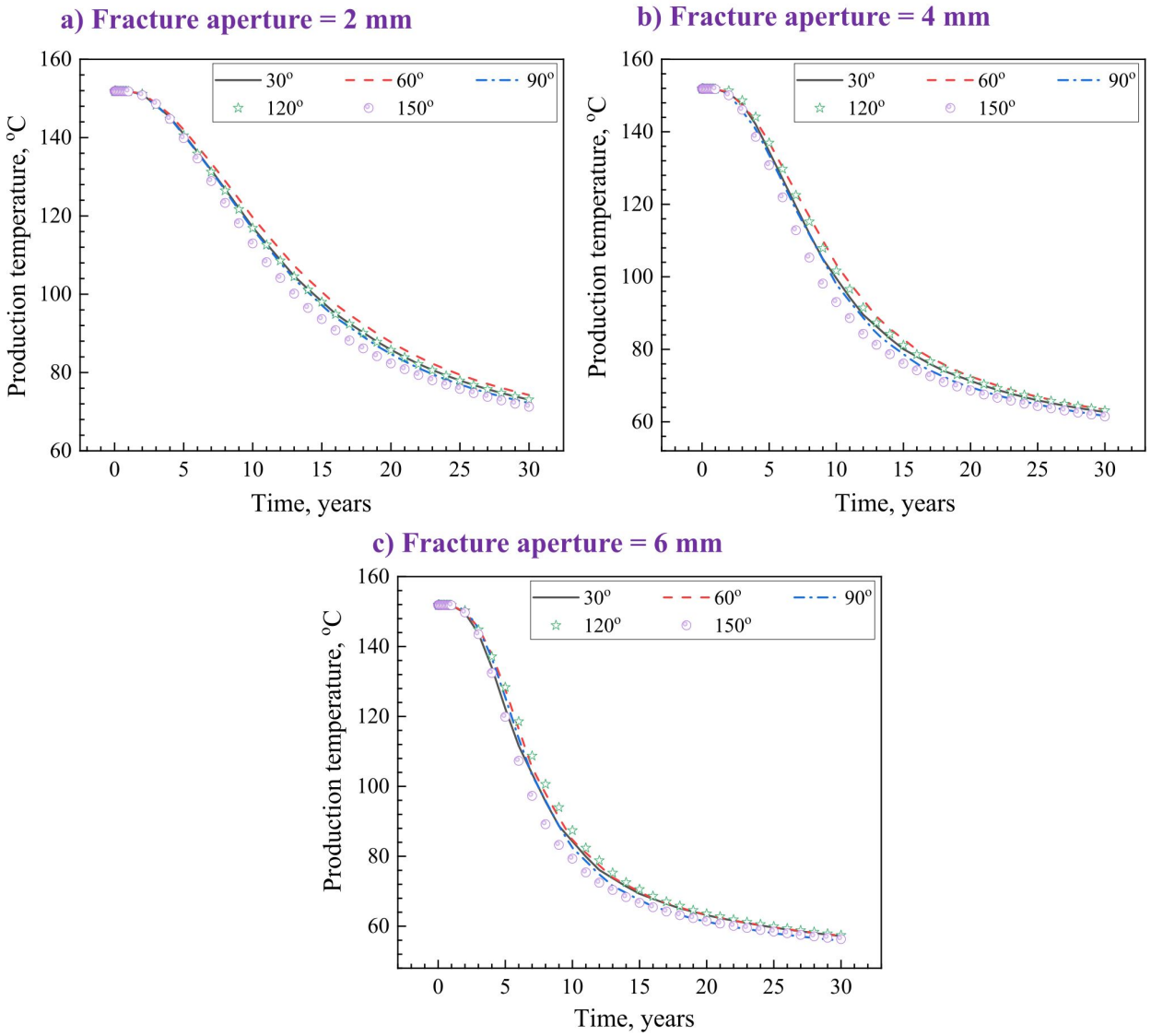


Figure 8: Impact of fracture angle on production temperature.

*4.3. Evolution of strain*

The importance of stains generated due to thermal and mechanical variations in the reservoir extensively studied. Figure 10 represents the spatial and temporal disparity of both thermal and mechanical strains. The volume of rock matrix variation due to the temperature difference is called thermal strain. It was found that the strain generated due to temperature variation is highly active near the hydraulic fracture and injection well. Maximum thermal strain was identified neighbouring the injection well and lowest observed at the production well (Figure 10*a* and 10*b*). It was found that the, minimum strain generated due to mechanical variation was found in the low temperature zone (Figure 10*c* and 10*d*). Thus, strains generated due to thermal variation is more active in the low-temperature zone, and geomechanical stresses were influential in the rest of the area (i.e., away from the low temperature zone). The thermal and mechanical strain dominated region in the reservoir is

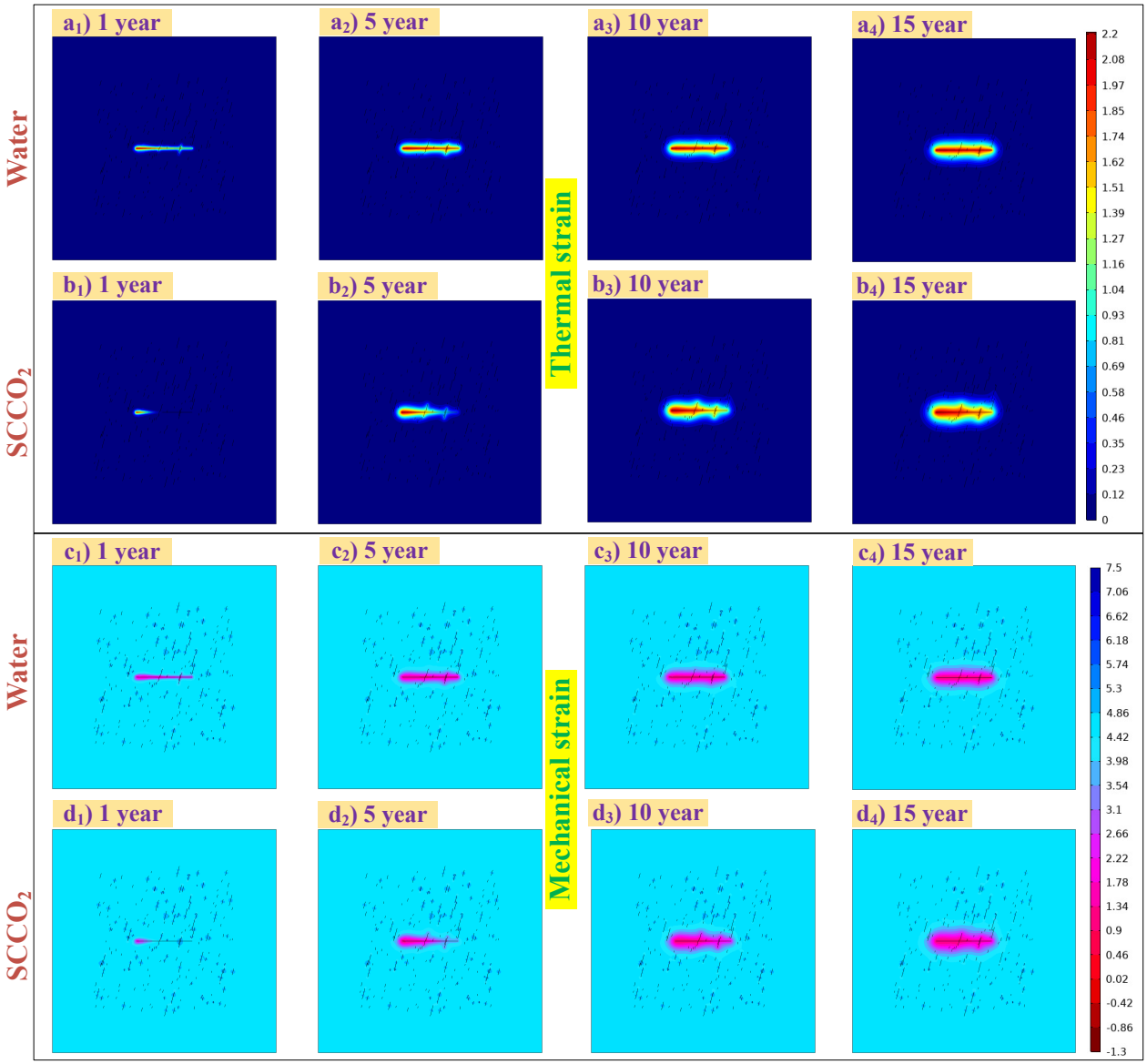


Figure 10: Comparison of $SCCO_2$ and water as geofluids on thermal and mechanical strains ($\times 10^{-3}$) at natural fracture orientation of $75^o$.

highly reliant on the on the type of geofluid (Figure 10). Low temperature region is more prominent in when water is used as geofluid compared to the $SCCO_2$. Due to this the when using water, thermal strains are more significant in in the low temperature region compared to $SCCO_2$. Thus, thermal, and mechanical are highly influenced by the type of fluid.

### *4.4. Neural Networks Model for Geothermal reservoirs*

#### *4.4.1. Neural Networks*

Neural networks have been employed successfully in the medical, engineering, economics, mathematics and other fields for the identification of patterns, sound, speech, forecasting of stock market, rain, weather and etc. From the last few years, application of neural network in the geoscience and hydrocarbon sectors gained more attraction. Which includes,

prediction of crude oil production, rock properties, and recognition of seismic pattern, etc. [1, 40, 41, 42, 43, 44, 49, 50]. Neural networks are the non-traditional tactics in which they are accomplished to study system of solutions relatively than being programmed to model a specific problem in the normal way. Neural networks are extensively recognized as a technology provides a substitute way to address the complex problems and also an alternative to the complex rules. Neural networks are able to learn the key information from the multi-layered information provided in the form data. Neural networks (NNs) contains an input layer (IL), output layer (OL) and these are connected with the series of hidden layer(HL)s. Each HL is having number of neurons which receives the information from the previous neuron for processing.

*4.4.2. Mathematical Model Based on FCN to predict production temperature*

In this work, time series model was developing using the FCN model. The FCN model is utilized to develop a mathematical model to predict the production temperature using the influencing parameters. The structure and algorithm of FCN are provided as follows:

**Computational geometry**: A new computation geometry was designed for the hybrid DNN and time series model and is presented in Figure 2*b*. complex natural fracture network was created using power law and Fisher distributions presented in section 3.2. The natural fracture aperture ranging from 0.1 mm to 5 mm, length of natural fractures varied from 1 m to 50 m, and orientations varied from 0° to 165°. Same initial and boundary conditions were imposed expect the injection temperature, fracture aperture, fracture length, inj/prod velocity and these are considered as influencing parameters in the present work.

**Sampling:** Training data generated by utilizing the design of experimentation technique. Response surface methodology (RSM) was applied for the qualitative numerical experimentation. Total four influencing parameters were identified and Response surface methodology was designed thirty numerical experimentation's. Table 2 provides the minimum and maximum ranges of influencing parameters and Table 3 illustrates the designed qualitative experimentation to conduct the numerical simulations. These numerical experimentation's will provide adequate training and validated data set FCN model to evaluate the influence of input parameter on the temperature at the production well.

**Input Layer**: The input layer includes five nodes which includes the injection temperature, fracture aperture, fracture length, inj/prod velocity, and time.

**Output layer**: Output layer consists of one output node and it is production temperature, it is obtained from the numerical simulations.

**Hidden layer (HL)**: The number of input nodes in the input layers varies and it is depending upon the problem statement. It is not possible to use the same architecture for all the problem statements. For the optimum architecture of the FCN, for better accuracy we utilized 30 neurons and on bias in the present work.

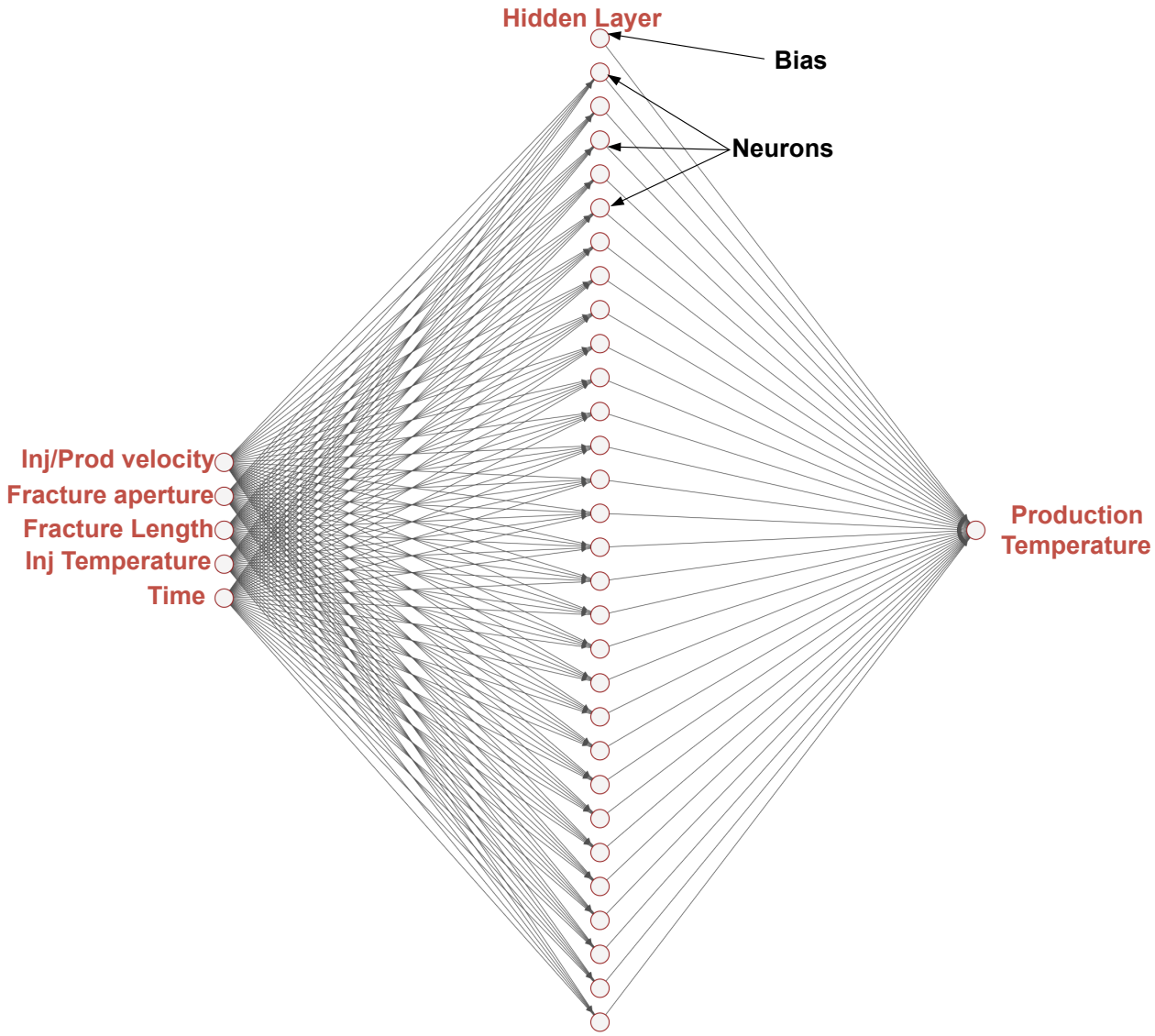


Figure 11: Schematic of the FCN model to predict the production temperature.

Table 2: Influencing parameter and its ranges with units

| Name of Factor | Unit | Lower limit | Higher limit |
|---|---|---|---|
| Injection Temperature | °C | 35 | 45 |
| Fluid injection/production velocity | m/s | 0.025 | 0.05 |
| Fracture aperture | mm | 2 | 6 |
| Fracture length | m | 200 | 300 |

**Objective/Loss functions**: DNN models were employed to estimate the temporal changes occur in temperature at the production well. There is a diversity of error calculation tools available in the design of DNN models. In the present work we applied Average

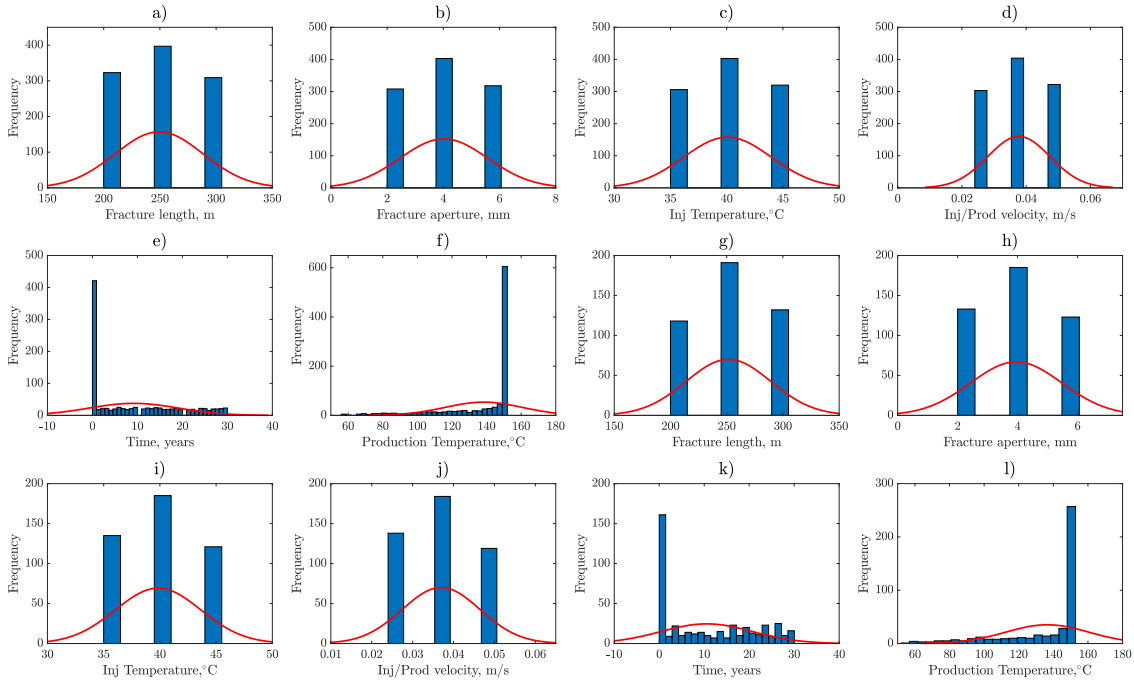


Figure 12: Histogram of training (a to f), testing (g to l)

absolute percentage of error (AAPE), root mean square error (RMSE), and coefficient of determination ($R^2$) as error estimation (loss) functions. The equations from Eq. (45) to Eq. (47) represents the loss functions used in the design of DNN models.

$$AAPE = \frac{100}{n_{TR} T_{p-data}} \Sigma_{i=1}^{n_{TR}} (T_{p-DNN} - T_{p-data}) \tag{45}$$

$$RMSE = \sqrt{\Sigma_{i=1}^{n_{TR}} \frac{(T_{p-DNN} - T_{p-data})^2}{n_{TR}}} \tag{46}$$

$$R^2 = 1 - \frac{\Sigma_{i=1}^{n_{TR}} (T_{p-data} - T_{p-DNN})^2}{\Sigma_{i=1}^{n_{TR}} (T_{p-DNN} - T_{avg,p-data})^2} \tag{47}$$

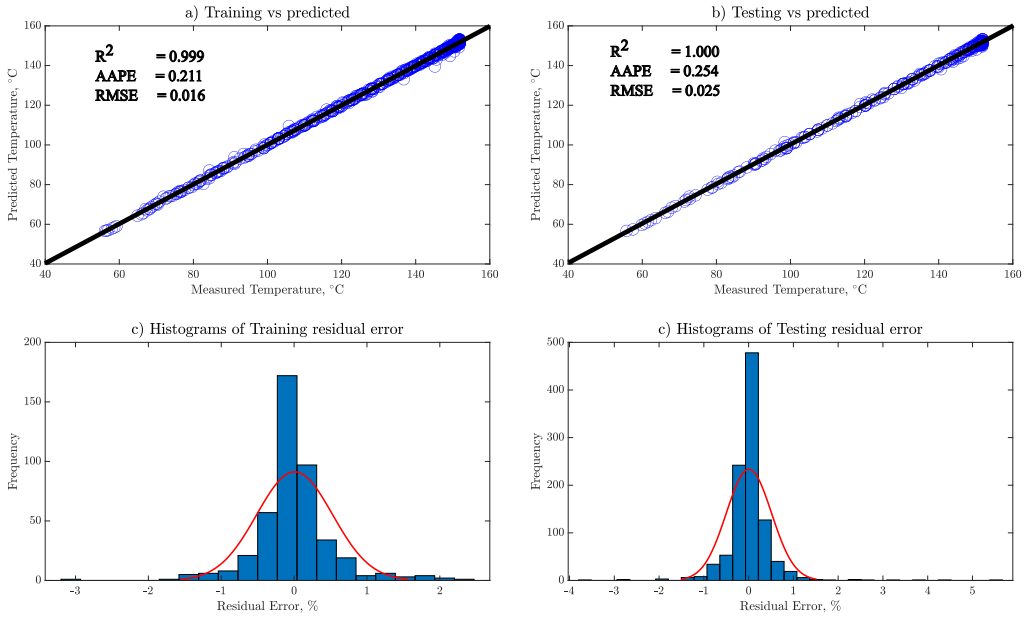


Figure 13: Production temperature of numerical simulations verses DNN model predicted with residual error histograms

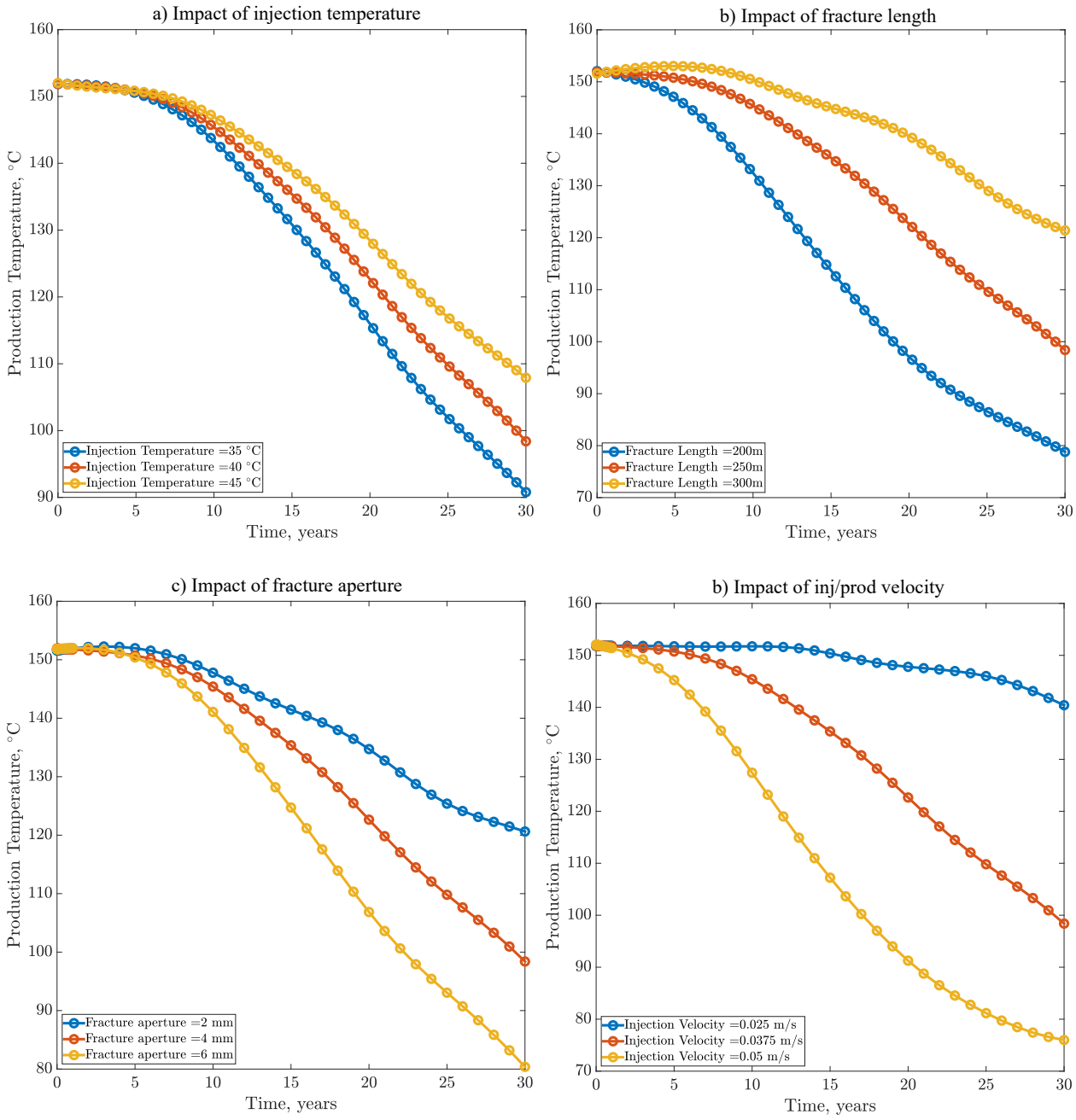


Figure 14: Impact of influencing parameters on the production temperature (i.e., results from the Eq (51)).

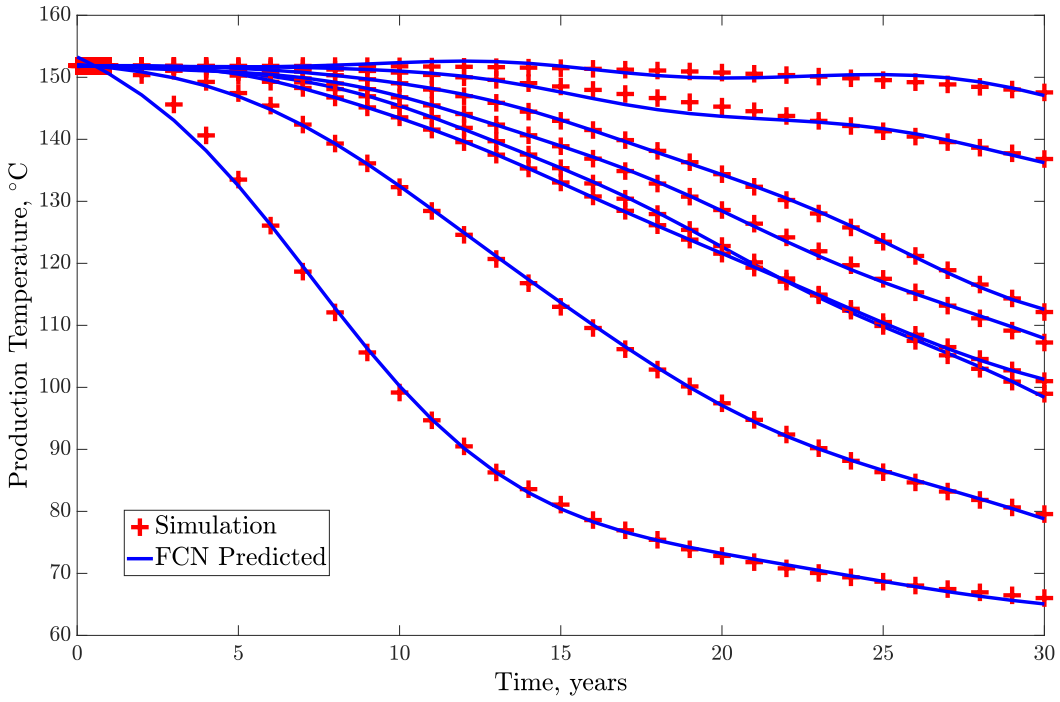


Figure 15: Comparison of simulated results with the equation (i.e., Eq. (51)) developed from the FCN .

Table 3: Qualitative numerical experimentation's for deep neural networks

| **Sl. No** | **Hydraulic Fracture length,** $m$ | **Hydraulic Fracture aperture,** $mm$ | **Injection Temperature,**$^{\circ}C$ | **Injection/ production velocity ,** $m/s$ |
|---|---|---|---|---|
| 1 | 250 | 4 | 40 | 0.0375 |
| 2 | 200 | 2 | 45 | 0.025 |
| 3 | 300 | 6 | 45 | 0.025 |
| 4 | 200 | 6 | 45 | 0.05 |
| 5 | 300 | 2 | 35 | 0.05 |
| 6 | 200 | 4 | 40 | 0.0375 |
| 7 | 250 | 4 | 45 | 0.0375 |
| 8 | 200 | 6 | 45 | 0.025 |
| 9 | 300 | 4 | 40 | 0.0375 |
| 10 | 250 | 4 | 40 | 0.0375 |
| 11 | 300 | 6 | 35 | 0.025 |
| 12 | 200 | 2 | 35 | 0.025 |
| 13 | 250 | 4 | 40 | 0.025 |
| 14 | 250 | 4 | 40 | 0.0375 |
| 15 | 250 | 6 | 40 | 0.0375 |
| 16 | 300 | 6 | 35 | 0.05 |
| 17 | 200 | 6 | 35 | 0.05 |
| 18 | 250 | 4 | 40 | 0.05 |
| 19 | 250 | 4 | 40 | 0.0375 |
| 20 | 250 | 2 | 40 | 0.0375 |
| 21 | 300 | 2 | 45 | 0.05 |
| 22 | 250 | 4 | 40 | 0.0375 |
| 23 | 200 | 2 | 35 | 0.025 |
| 24 | 300 | 6 | 45 | 0.05 |
| 25 | 200 | 2 | 45 | 0.05 |
| 26 | 200 | 6 | 35 | 0.025 |
| 27 | 250 | 4 | 40 | 0.0375 |
| 28 | 250 | 4 | 35 | 0.0375 |
| 29 | 300 | 2 | 35 | 0.025 |
| 30 | 300 | 2 | 45 | 0.025 |

**Mathematical Equation to Estimate Production Temperature**:

The structure of the fully connected neural network is presented in Figure 11. The distribution of the input and output parameters used in the training and testing were presented in the Figure 12. Figure 13$a$ depicts the cross plots of training and testing data, which shows

the greater accuracy in the prediction of the production temperature. The residual errors were accumulated with in the -2 to 2 for both training and testing data (Figure 13). A mathematical equation was developed using the above FCN model with influencing parameters. The Hidden layer neuron utilizing its weight $w_1$, and bias $b_1$, and the mathematical expression is presented in Eq (48).

$$\sigma_{tf,L}\left(\Sigma_{j=1}^{N_p} w_{1,j}x_j + b_1\right) \tag{48}$$

The output of the whole network will be expressed in Eq (49)

$$\mu_p(\varphi) = \sigma_{tf,0}\left[\Sigma_{i=1}^{N_h} w_{2,i}\sigma_{tf,L}\left(\Sigma_{j=1}^{N_p} w_{1,j}x_j + b_1\right) + b_2\right] \tag{49}$$

Here, $\sigma_{tf,L}(x) = \left(\frac{2}{1+e^{-2x}} - 1\right)$, and $\sigma_{tf,0}(x) = x$. The proposed equation of FCN of the production temperature can be written more specifically as in Eq (50)

$$T_{prod} = 103.75 - 48.05T_{prod,n} \tag{50}$$

The equation for the $T_{prod,n}$ is given in Eq (51)

$$T_{prod,n} = \sigma_{tf,0}\left[\Sigma_{i=1}^{N_h} w_{2,i}\sigma_{tf,L}(X_1) + b_2\right] \tag{51}$$

$$X_1 = w_{1,_{i,1}}L_{f,n} + w_{1,_{i,2}}d_{afrc,n} + w_{1,_{i,3}}T_{inj,n} + w_{1,_{i,4}}v_{inj/prod,n} + w_{1,_{i,5}}t_n + b_{1,_i} \tag{52}$$

The expressions for the normalized terms such as $L_{f,n}$, $d_{afrc,n}$, $T_{inj,n}$, $v_{inj/prod,n}$, and $t_n$ were presented from Eq (53) to Eq (57) .

$$L_{f,n} = 5 - 0.02L_f \tag{53}$$

$$d_{afrc,n} = 2 - 0.5d_{afrc} \tag{54}$$

$$T_{inj,n} = 8 - 0.2T_{inj} \tag{55}$$

$$v_{inj/prod,n} = 3 - 80v_{inj/prod} \tag{56}$$

$$t_n = 1 - 0.066t \tag{57}$$

Here, $L_f$ in m, $d_{afrc}$ in mm, $T_{inj}$ in °C, $v_{inj/prod}$ in m/s, and $t$ is in years. The developed mathematical model with FCN showing a greater accuracy with the simulated results. The impact of influencing parameters on the production temperature was depicted in the Figure 14 and similar impact was observed from the simulation results (i.e., Figure 7). The accuracy of the developed mathematical model was also checked with the ten random scenarios and comped with the simulated results. From the Figure 15, it was found the the developed mathematical model was showing the similar results with the simulated results. Thus, the developed mathematical model can be utilized to predict the temporal evolution of the production temperature of a fractured geothermal reservoir with in the desired limits.

Table 4: Weights and Biases of the Optimized neural network model

| Neurons | Weights between Input and Hidden Layer ($w_1$) | | | | | Weights between Hidden and Output Layer ($w_2$) | Bias between Input and Hidden Layer ($b_1$) | Bias between Hidden and Output Layer ($b_2$) |
|---|---|---|---|---|---|---|---|---|
| | $L_{f,n}$ | $d_{afrc,n}$ | $T_{inj,n}$ | $v_{inj/prod,n}$ | $t_n$ | | | |
| 1 | 0.530 | −0.588 | 0.162 | −2.465 | −1.944 | 0.438 | 2.754 | 0.745 |
| 2 | −0.846 | −0.965 | −0.278 | 1.005 | −0.783 | −0.319 | 3.745 | |
| 3 | 1.316 | 1.576 | 1.926 | −0.222 | −2.134 | 0.052 | 0.785 | |
| 4 | −0.892 | 3.643 | −1.015 | −2.038 | 0.471 | 0.067 | 2.110 | |
| 5 | −0.003 | 1.164 | −3.465 | −2.910 | −0.120 | −0.075 | 2.948 | |
| 6 | −1.988 | 3.694 | 0.281 | 0.187 | 1.075 | −0.039 | 1.139 | |
| 7 | −0.113 | −1.434 | −2.841 | 1.038 | −0.003 | −0.068 | −1.059 | |
| 8 | 1.363 | −1.940 | 3.105 | 1.271 | 2.411 | 0.068 | −1.272 | |
| 9 | −0.047 | −0.007 | 0.042 | 0.933 | 2.952 | −0.178 | 0.766 | |
| 10 | −1.546 | −3.237 | −0.747 | −0.380 | −0.062 | −0.213 | −0.978 | |
| 11 | −2.173 | 0.386 | −1.199 | 1.140 | −1.371 | −0.069 | 1.791 | |
| 12 | 1.325 | 1.914 | −1.833 | 0.328 | −0.210 | −0.211 | −1.293 | |
| 13 | 1.191 | 1.767 | 2.874 | −0.609 | −1.482 | −0.164 | −0.574 | |
| 14 | 0.802 | −3.961 | −0.387 | 0.801 | 2.324 | 0.141 | −4.276 | |
| 15 | 0.430 | −0.183 | 0.043 | −1.651 | −2.571 | 0.311 | 0.895 | |
| 16 | −3.720 | 1.981 | 1.765 | 1.129 | −1.357 | 0.111 | −0.126 | |
| 17 | 0.243 | −1.162 | −2.589 | 0.313 | −2.034 | 0.042 | −0.357 | |
| 18 | 1.224 | −0.374 | −1.156 | 3.432 | −1.421 | 0.151 | 0.131 | |
| 19 | 2.476 | 1.300 | −0.107 | −3.223 | 1.036 | 0.130 | 0.168 | |
| 20 | −0.636 | −2.689 | −0.092 | 1.677 | 0.377 | −0.241 | 0.169 | |
| 21 | −2.487 | −3.579 | 1.644 | −0.786 | 2.596 | 0.056 | −0.291 | |
| 22 | 2.821 | 2.612 | −2.356 | −2.287 | 2.642 | 0.056 | 0.357 | |
| 23 | −2.151 | −1.937 | −0.682 | 1.946 | −0.090 | 0.345 | −1.162 | |
| 24 | 1.415 | 4.384 | 0.284 | −1.062 | −2.066 | −0.047 | 1.068 | |
| 25 | −0.662 | −0.183 | 2.816 | −0.777 | 4.132 | 0.016 | −1.602 | |
| 26 | 3.671 | −1.015 | 0.804 | −3.300 | −1.453 | 0.111 | 1.223 | |
| 27 | 4.935 | 0.070 | −1.298 | −1.427 | −2.790 | 0.105 | 3.398 | |
| 28 | 1.906 | 1.307 | 2.208 | −2.510 | −0.495 | 0.008 | 3.373 | |
| 29 | 0.163 | 2.684 | −2.063 | 1.999 | −0.598 | −0.185 | 3.304 | |
| 30 | −1.780 | 1.102 | 3.987 | −0.532 | −0.456 | −0.186 | 3.416 | |

## 5. Conclusions

In the present research work, we used the fully coupled THM model to examine the behaviour of geothermal reservoir. The dynamic behaviour of fluid, rock, and fracture properties were considered in the present work. The influence of natural fracture and its orientation is also examined effectively. COMSOL Multiphysics software was utilized in the present work for the numerical experimentation's using the THM model. The effect of $SCCO_2$ as geofluid for the heat extraction is also studied extensively and compared with the water as geofluid.

Temperature at the production well, and low-temperature zone in rock matrix are deliberately impacted by inj/prod velocity, aperture of hydraulic fracture, and natural fracture orientation. Production temperature is declines with advancement in time and inj/prod velocity, and hydraulic fracture aperture. The comparison between water-EGS and $SCCO_2$-EGS system on the production temperature was determined and found $SCCO_2$-EGS system is providing promising results compared to water-EGS. Strain generated due to thermal drawdown is active at the low-temperature zone, and strain generated due to mechanical loads is substantial in the rest of the area. Natural fractures interaction with the hydraulic fracture, and type of geofluid are influencing the production temperature, thermal strain, mechanical strains in the geothermal reservoir.

An FCN model was employed to forecast the temporal temperature at the production well as a function of injection temperature, inj/prod velocity, HF aperture, and HF length. Response surface methodology was utilized to design the numerical experimentation's with-

out temporal constituent. A mathematical equation was developed to predict the temporal variation of temperature at the production well to a desired level using FCN. Therefore, the developed numerical simulations with FCN model can be a useful tool to investigative the temporal evolution of production temperature with higher accuracy.

## Credit authorship contribution statement

**Manojkumar Gudala**: Conceptualization, Methodology, Software, Validation, Formal analysis, Writing – original draft, Writing – review & editing, Investigation. **Bicheng Yan**: Software, Formal analysis, Resources, Writing – review & editing, Funding acquisition. **Shuyu Sun**: Funding support, study conceptualization, methodology development and manuscript revision. **Suresh Kumar Govindarajan**: Study conceptualization, computational analysis, manuscript revision. **Zeeshan Tariq**: Study conceptualization, computational analysis, manuscript revision. **Zhen Xu** :Software, Writing – review & editing, Investigation.

## Declaration of competing interest

The authors declare that they have no known competing financial interests or personal relationships that could have appeared to influence the work reported in this paper.

## Acknowledgements

**Manojkumar Gudala**, **Zeeshan Tariq**, **Zhen Xu** and **Bicheng Yan** thanks for the Research Funding from King Abdullah University of Science and Technology (KAUST), Saudi Arabia through the grants BAS/1/1423-01-01 and FCC/1/4491-22-01; **Manojkumar Gudala** and **Shuyu Sun** thanks for the Research Funding from King Abdullah University of Science and Technology (KAUST), Saudi Arabia through the grants BAS/1/1351-01-01 and URF/1/4074-01-01;**Manojkumar Gudala** and **Suresh Kumar Govindarajan** gratefully acknowledge financial support from the Indian Institute of Technology–Madras.

## Nomenclature

$d_{afrc,n}$ Normalized fracture aperture

$L_{f,n}$ Normalized fracture length

$N_p$ Number of neurons

$t_n$ Normalized time

$T_{inj,n}$ Normalized injection temperature

$v_{inj/prod,n}$ Normalized injection/production velocity

$w_{1,j}$ Weights in hidden layer

$x_j$ Parameters

$\alpha_b$ Biot-Wills coefficient

$\alpha_T$ Coefficient of thermal expansion

$\Delta\varepsilon_T$ Thermal strain

$\Delta\varepsilon_{vol}$ Change in volumetric strain

$\Delta T$ Change in temperature

$\frac{\partial\varepsilon_{vol}}{\partial t}$ Rate of change in volumetric strain of the porous matrix

$\kappa_{frc0}$ Initial fracture permeability

$\kappa_{frc}$ Fracture permeability

$\kappa_{mat}$ Rock permeability

$\lambda_{eff}$ Effective thermal conductivity

$\lambda_{fl}$ Thermal conductivity of fluid

$\lambda_{mat}$ Thermal conductivity of matrix

$\mu_{fl}$ Viscosity of the fluid

$\nabla_{Tn}$ Gradient is measured on the tangential plane of fracture

$\nu_{frc}$ Poisson's ratio of fracture

$\phi_{mat}$ Porosity of matrix

$\phi_{ini}$ Initial porosity of matrix

$\rho_{fl}$ Density of fluid

$\rho_{mat}$ rock density

$\sigma_n$ Normal stress acting on fracture

$\sigma^*$ Normalizing constant (and it is considered as the initial reservoir pressure)

$a_1$ Constant

$b_1$ Constant

$C_n$ Coefficient and it is a function of initial porosity of formation and is equal to $5/\phi_i$

$C_{p,fl}$ Specific heat capacity of fluid

$C_{p,mat}$ Specific heat capacity of matrix

$d$ Fitting parameter (constant and equal to 1)

$d_A$ Damping constant per unit area

$d_{afrc}$ Fracture aperture

$E_i$ Initial elastic modulus

$E_{frc}$ Elastic modulus of fracture

$K_A$ Spring constant

$K_d$ Drained bulk modules

$k_n$ Stiffness in the normal direction

$k_s$ Shear Stiffness

$K_{fl}$ Fluid bulk modules

$M$ Biot's modulus

$p$ pressure

$p_{frc}$ Pressure in fracture

$q_m$ Source/sink term which couple both matrix and fracture with mechanics

$Q_{fracT}$ Source/sink terms fracture

$q_{frc}$ Flow rate in fractures

$Q_{matT}$ Source term of matrix

$sigma_{tf,L}$ Activation function

$T$ Temperature

$t$ Time

$T_{avg,p-data}$ Mean production temperature of the given data

$T_{p-data}$ Production temperature of the from the training data

$T_{p-DNN}$ Production temperature predicted from the DNN model

$u_0$ Initial displacement of fracture

$u_d$ Displacement in downside of fracture

$u_u$ Displacement in upside of fracture

$u_{dlm}$ Darcy's Velocity

$u_{frc}$ Darcy's velocity in fracture

## References


[1] Ling Zhou, Yanjun Zhang, Zhongjun Hu, Ziwang Yu, Yinfei Luo, Yude Lei, Honglei Lei, Zhihong Lei, and Yueqiang Ma. Analysis of influencing factors of the production performance of an enhanced geothermal system (egs) with numerical simulation and artificial neural network (ann). *Energy and Buildings*, 200:31–46, 2019.

[2] Hannes Hofmann, Tayfun Babadagli, Jeoung Seok Yoon, Guido Blöcher, and Günter Zimmermann. A hybrid discrete/finite element modeling study of complex hydraulic fracture development for enhanced geothermal systems (egs) in granitic basements. *Geothermics*, 64:362–381, 2016.

[3] Donald W Brown. A hot dry rock geothermal energy concept utilizing supercritical $co_2$ instead of water. In *Proceedings of the twenty-fifth workshop on geothermal reservoir engineering, Stanford University*, pages 233–238. Citeseer, 2000.

[4] James Biagi, Ramesh Agarwal, and Zheming Zhang. Simulation and optimization of enhanced geothermal systems using $co_2$ as a working fluid. *Energy*, 86:627–637, 2015.

[5] Fu-Zhen Zhang, Rui-Na Xu, and Pei-Xue Jiang. Thermodynamic analysis of enhanced geothermal systems using impure $co_2$ as the geofluid. *Applied Thermal Engineering*, 99: 1277–1285, 2016.

[6] Chunjian Pan, Oscar Chávez, Carlos E Romero, Edward K Levy, Alicia Aguilar Corona, and Carlos Rubio-Maya. Heat mining assessment for geothermal reservoirs in mexico using supercritical $co_2$ injection. *Energy*, 102:148–160, 2016.

[7] Liang Zhang, Xin Li, Yin Zhang, Guodong Cui, Chunyang Tan, and Shaoran Ren. $co_2$ injection for geothermal development associated with egr and geological storage in depleted high-temperature gas reservoirs. *Energy*, 123:139–148, 2017.

[8] Lehua Pan, Barry Freifeld, Christine Doughty, Steven Zakem, Ming Sheu, Bruce Cutright, and Tracy Terrall. Fully coupled wellbore-reservoir modeling of geothermal heat extraction using $co_2$ as the working fluid. *Geothermics*, 53:100–113, 2015.

[9] P. Olasolo, M. C. Juárez, M. P. Morales, Sebastiano Damico, and I. A. Liarte. Enhanced geothermal systems (EGS): A review. *Renewable and Sustainable Energy Reviews*, 56: 133–144, 2016. ISSN 18790690. doi: 10.1016/j.rser.2015.11.031.

[10] Shunde Yin, Maurice B Dusseault, and Leo Rothenburg. Coupled thmc modeling of co2 injection by finite element methods. *Journal of Petroleum Science and Engineering*, 80 (1):53–60, 2011.

[11] Fu-Zhen Zhang, Pei-Xue Jiang, and Rui-Na Xu. System thermodynamic performance comparison of $co_2$-egs and water-egs systems. *Applied thermal engineering*, 61(2):236–244, 2013.

[12] Nagasree Garapati, Jimmy B Randolph, and Martin O Saar. Brine displacement by $co_2$, energy extraction rates, and lifespan of a $co_2$-limited $co_2$-plume geothermal (cpg) system with a horizontal production well. *Geothermics*, 55:182–194, 2015.

[13] Liang Zhang, Guodong Cui, Yin Zhang, Bo Ren, Shaoran Ren, and Xiaohui Wang. Influence of pore water on the heat mining performance of supercritical $co_2$ injected for geothermal development. *Journal of $CO_2$ Utilization*, 16:287–300, 2016.

[14] Chunjian Pan, Carlos E Romero, Edward K Levy, Xingchao Wang, Carlos Rubio-Maya, and Lehua Pan. Fully coupled wellbore-reservoir simulation of supercritical $co_2$ injection from fossil fuel power plant for heat mining from geothermal reservoirs. *Journal of CO2 Utilization*, 27:480–492, 2018.

[15] Zhan-qing Qu, Wei Zhang, and Tian-kui Guo. Influence of different fracture morphology on heat mining performance of enhanced geothermal systems based on comsol. *International Journal of Hydrogen Energy*, 42(29):18263–18278, 2017.

[16] Feng Luo, Rui-Na Xu, and Pei-Xue Jiang. Numerical investigation of fluid flow and heat transfer in a doublet enhanced geothermal system with $co_2$ as the working fluid ($co_2$–egs). *Energy*, 64:307–322, 2014.

[17] Chang-Long Wang, Wen-Long Cheng, Yong-Le Nian, Lei Yang, Bing-Bing Han, and Ming-Hou Liu. Simulation of heat extraction from $co_2$-based enhanced geothermal systems considering $co_2$ sequestration. *Energy*, 142:157–167, 2018.

[18] Tiankui Guo, Facheng Gong, Xiaozhi Wang, Qiang Lin, Zhanqing Qu, and Wei Zhang. Performance of enhanced geothermal system (egs) in fractured geothermal reservoirs with $co_2$ as working fluid. *Applied Thermal Engineering*, 152:215–230, 2019.

[19] Yuxiang Cheng, Yanjun Zhang, Ziwang Yu, Zhongjun Hu, and Yunxing Yang. An investigation on hydraulic fracturing characteristics in granite geothermal reservoir. *Engineering Fracture Mechanics*, 237:107252, 2020.

[20] AR Khoei, S Moallemi, and E Haghighat. Thermo-hydro-mechanical modeling of impermeable discontinuity in saturated porous media with x-fem technique. *Engineering Fracture Mechanics*, 96:701–723, 2012.

[21] Wenbo Huang, Wenjiong Cao, and Fangming Jiang. Heat extraction performance of egs with heterogeneous reservoir: A numerical evaluation. *International Journal of Heat and Mass Transfer*, 108:645–657, 2017.

[22] Ali Ranjbar, Hossein Hassani, Kourosh Shahriar, and Mohammad Javad Ameri Shahrabi. Thermo-hydro-mechanical modeling of fault discontinuities using zero-thickness interface element. *Journal of Rock Mechanics and Geotechnical Engineering*, 12(1):74–88, 2020.

[23] Teng Teng, Yixin Zhao, Feng Gao, JG Wang, and Wei Wang. A fully coupled thermo-hydro-mechanical model for heat and gas transfer in thermal stimulation enhanced coal seam gas recovery. *International Journal of Heat and Mass Transfer*, 125:866–875, 2018.

[24] Ying Xin, Zhixue Sun, Li Zhuang, Jun Yao, Kai Zhang, Dongyan Fan, Kelvin Bongole, Tong Wang, and Chuanyin Jiang. Numerical simulation of fluid flow and heat transfer in egs with thermal-hydraulic-mechanical coupling method based on a rough fracture model. *Energy Procedia*, 158:6038–6045, 2019.

[25] Quan Gan and Derek Elsworth. Production optimization in fractured geothermal reservoirs by coupled discrete fracture network modeling. *Geothermics*, 62:131–142, 2016.

[26] Yu-Chao Zeng, Neng-You Wu, Zheng Su, Xiao-Xing Wang, and Jian Hu. Numerical simulation of heat production potential from hot dry rock by water circulating through a novel single vertical fracture at desert peak geothermal field. *Energy*, 63:268–282, 2013.

[27] Don B Fox, Daniel Sutter, Koenraad F Beckers, Maciej Z Lukawski, Donald L Koch, Brian J Anderson, and Jefferson W Tester. Sustainable heat farming: Modeling extraction and recovery in discretely fractured geothermal reservoirs. *Geothermics*, 46:42–54, 2013.

[28] Anna Suzuki, Sergei A Fomin, Vladimir A Chugunov, Yuichi Niibori, and Toshiyuki Hashida. Fractional diffusion modeling of heat transfer in porous and fractured media. *International Journal of Heat and Mass Transfer*, 103:611–618, 2016.

[29] SN Pandey and Vikram Vishal. Sensitivity analysis of coupled processes and parameters on the performance of enhanced geothermal systems. *Scientific reports*, 7(1):1–14, 2017.

[30] Yating Wang and Guang Lin. Efficient deep learning techniques for multiphase flow simulation in heterogeneous porousc media. *Journal of Computational Physics*, 401: 108968, 2020. doi: https://doi.org/10.1016/j.jcp.2019.108968.

[31] Bicheng Yan, Dylan Robert Harp, Bailian Chen, Hussein Hoteit, and Rajesh J. Pawar. A gradient-based deep neural network model for simulating multiphase flow in porous media. *Journal of Computational Physics*, 463:111277, 2022. doi: https://doi.org/10.1016/j.jcp.2022.111277.

[32] Bicheng Yan, Bailian Chen, Dylan Robert Harp, Wei Jia, and Rajesh J. Pawar. A robust deep learning workflow to predict multiphase flow behavior during geological $co_2$ sequestration injection and post-injection periods. *Journal of Hydrology*, 607:127542, 2022. doi: https://doi.org/10.1016/j.jhydrol.2022.127542.

[33] Bicheng Yan, Dylan Robert Harp, Bailian Chen, and Rajesh Pawar. A physics-constrained deep learning model for simulating multiphase flow in 3d heterogeneous porous media. *Fuel*, 313:122693, 2022. doi: https://doi.org/10.1016/j.fuel.2021.122693.

[34] Zeeshan Tariq, Murtada Saleh Aljawad, Amjed Hasan, Mobeen Murtaza, Emad Mohammed, Ammar El-Husseiny, Sulaiman A Alarifi, Mohamed Mahmoud, and Abdulazeez Abdulraheem. A systematic review of data science and machine learning applications to the oil and gas industry. *Journal of Petroleum Exploration and Production Technology*, 11(12):4339–4374, 2021.

[35] K Aminian, S Ameri, A Oyerokun, and B Thomas. Prediction of flow units and permeability using artificial neural networks. In *SPE Western Regional/AAPG Pacific Section Joint Meeting*. OnePetro, 2003.

[36] Raoof Gholami, Ali Moradzadeh, Shahoo Maleki, Saman Amiri, and Javid Hanachi. Applications of artificial intelligence methods in prediction of permeability in hydrocarbon reservoirs. *Journal of Petroleum Science and Engineering*, 122:643–656, 2014.

[37] Teslim Olayiwola, Zeeshan Tariq, Abdulazeez Abdulraheem, and Mohamed Mahmoud. Evolving strategies for shear wave velocity estimation: smart and ensemble modeling approach. *Neural Computing and Applications*, 33(24):17147–17159, 2021.

[38] Salaheldin Elkatatny, Mohamed Mahmoud, Zeeshan Tariq, and Abdulazeez Abdulraheem. New insights into the prediction of heterogeneous carbonate reservoir permeability from well logs using artificial intelligence network. *Neural Computing and Applications*, 30(9):2673–2683, 2018.

[39] Zeeshan Tariq, Mohamed Mahmoud, and Abdulazeez Abdulraheem. An intelligent data-driven model for dean–stark water saturation prediction in carbonate rocks. *Neural Computing and Applications*, 32(15):11919–11935, 2020.

[40] M Adibifard, SAR Tabatabaei-Nejad, and E Khodapanah. Artificial neural network (ann) to estimate reservoir parameters in naturally fractured reservoirs using well test data. *Journal of Petroleum Science and Engineering*, 122:585–594, 2014.

[41] Yongchao Xue, Linsong Cheng, Jianye Mou, and Wenqi Zhao. A new fracture prediction method by combining genetic algorithm with neural network in low-permeability reservoirs. *Journal of Petroleum Science and Engineering*, 121:159–166, 2014.

[42] Pejman Tahmasebi and Ardeshir Hezarkhani. A fast and independent architecture of artificial neural network for permeability prediction. *Journal of Petroleum Science and Engineering*, 86:118–126, 2012.

[43] Mohsen Saemi, Morteza Ahmadi, and Ali Yazdian Varjani. Design of neural networks using genetic algorithm for the permeability estimation of the reservoir. *Journal of Petroleum Science and Engineering*, 59(1-2):97–105, 2007.

[44] Manojkumar Gudala and Suresh Kumar Govindarajan. Numerical investigations on a geothermal reservoir using fully coupled thermo-hydro-geomechanics with integrated RSM-machine learning and ARIMA models. *Geothermics*, 96(May):102174, 2021. ISSN 03756505. doi: 10.1016/j.geothermics.2021.102174. URL `https://doi.org/10.1016/j.geothermics.2021.102174`.

[45] Zeeshan Tariq, Mobeen Murtaza, Mohamed Mahmoud, Murtada Saleh Aljawad, and Muhammad Shahzad Kamal. Machine learning approach to predict the dynamic linear swelling of shales treated with different waterbased drilling fluids. *Fuel*, 315:123282, 2022.

[46] Mahmoud Desouky, Zeeshan Tariq, Murtada Saleh Aljawad, Hamed Alhoori, Mohamed Mahmoud, and Abdulazeez Abdulraheem. Machine learning-based propped fracture conductivity correlations of several shale formations. *ACS omega*, 6(29):18782–18792, 2021.

[47] Zeeshan Tariq, Abdulazeez Abdulraheem, Mohamed Mahmoud, and Adil Ahmed. A rigorous data-driven approach to predict poisson's ratio of carbonate rocks using a functional network. *Petrophysics-The SPWLA Journal of Formation Evaluation and Reservoir Description*, 59(06):761–777, 2018.

[48] Zeeshan Tariq, Mohamed Mahmoud, and Abdulazeez Abdulraheem. Core log integration: a hybrid intelligent data-driven solution to improve elastic parameter prediction. *Neural Computing and Applications*, 31(12):8561–8581, 2019.

[49] Sachchida Nand Pandey and M Singh. Artificial neural network to predict the thermal drawdown of enhanced geothermal system. *Journal of Energy Resources Technology*, 143(1), 2021.

[50] Soteris A Kalogirou, Georgios A Florides, Panayiotis D Pouloupatis, Ioannis Panayides, Josephina Joseph-Stylianou, and Zomenia Zomeni. Artificial neural networks for the generation of geothermal maps of ground temperature at various depths by considering land configuration. *Energy*, 48(1):233–240, 2012.

[51] Hikmet Esen and Mustafa Inalli. Modelling of a vertical ground coupled heat pump system by using artificial neural networks. *Expert Systems with Applications*, 36(7): 10229–10238, 2009.

[52] Halldora Gudmundsdottir and Roland N Horne. Prediction modeling for geothermal reservoirs using deep learning. In *45th workshop on geothermal reservoir engineering. Stanford, California: Stanford University*, pages 1–12, 2020.

[53] Zhangxin Chen, Guanren Huan, and Yuanle Ma. *Computational methods for multiphase flows in porous media*. SIAM, 2006.

[54] Maurice A Biot. General theory of three-dimensional consolidation. *Journal of applied physics*, 12(2):155–164, 1941.

[55] Maurice A Biot. Theory of elasticity and consolidation for a porous anisotropic solid. *Journal of applied physics*, 26(2):182–185, 1955.

[56] Sanbai Li, Xia-Ting Feng, Dongxiao Zhang, and Huiying Tang. Coupled thermo-hydro-mechanical analysis of stimulation and production for fractured geothermal reservoirs. *Applied Energy*, 247:40–59, 2019.

[57] Guihong Liu, Hai Pu, Zhihong Zhao, and Yanguang Liu. Coupled thermo-hydro-mechanical modeling on well pairs in heterogeneous porous geothermal reservoirs. *Energy*, 171:631–653, 2019.

[58] Tiankui Guo, Songjun Tang, Jiang Sun, Facheng Gong, Xiaoqiang Liu, Zhanqing Qu, and Wei Zhang. A coupled thermal-hydraulic-mechanical modeling and evaluation of geothermal extraction in the enhanced geothermal system based on analytic hierarchy process and fuzzy comprehensive evaluation. *Applied Energy*, 258:113981, 2020.

[59] Bérénice Vallier, Vincent Magnenet, Jean Schmittbuhl, and Christophe Fond. Thm modeling of hydrothermal circulation at rittershoffen geothermal site, france. *Geothermal Energy*, 6(1):1–26, 2018.

[60] Tony T Freeman, Rick J Chalaturnyk, and Igor I Bogdanov. Fully coupled thermo-hydro-mechanical modeling by comsol multiphysics, with applications in reservoir geomechanical characterization. In *COMSOL Conf*, pages 9–11, 2008.

[61] Tony T Freeman, Rick J Chalaturnyk, and Igor I Bogdanov. Thm modeling for reservoir geomechanical applications. In *Comsol Conference*, 2008.

[62] LIU Jianxin. *A Porosity-Based Model for Coupled Thermal-Hydraulic-Mechanical Processes*. PhD thesis, The University of Western Australia, 2009.

[63] Stephen A Miller. Modeling enhanced geothermal systems and the essential nature of large-scale changes in permeability at the onset of slip. *Geofluids*, 15(1-2):338–349, 2015.

[64] Amin Touhidi-Baghini. *Absolute permeability of McMurray formation oil sands at low confining stresses*. PhD thesis, University of Alberta, 1998.

[65] COMSOL Multiphysics. Subsurface flow module user's guide. *Version: COMSOL*, 5, 2018.

[66] Yang Wang, Tuo Li, Yun Chen, and Guowei Ma. A three-dimensional thermo-hydro-mechanical coupled model for enhanced geothermal systems (egs) embedded with discrete fracture networks. *Computer Methods in Applied Mechanics and Engineering*, 356: 465–489, 2019.

[67] Danijela Šijačić and Peter A Fokker. Thermo-hydro-mechanical modeling of egs using comsol multiphysics. In *Fourtieth Workshop on Geothermal Reservoir Engineering*, page 52, 2015.

[68] Qinghua Lei, Nima Gholizadeh Doonechaly, and Chin-Fu Tsang. Modelling fluid injection-induced fracture activation, damage growth, seismicity occurrence and connectivity change in naturally fractured rocks. *International Journal of Rock Mechanics and Mining Sciences*, 138:104598, 2021.

[69] Reza Sanaee, Gbenga F Oluyemi, Mamdud Hossain, and MB Oyeneyin. Fracture-matrix flow partitioning and cross flow: numerical modeling of laboratory fractured core flood. In *Proceedings of the 2012 COMSOL conference, Milan, 10–12 October 2012*, 2012.

[70] Baptiste Lepillier, Alexandros Daniilidis, Nima Doonechaly Gholizadeh, Pierre-Olivier Bruna, Juliane Kummerow, and David Bruhn. A fracture flow permeability and stress dependency simulation applied to multi-reservoirs, multi-production scenarios analysis. *Geothermal Energy*, 7(1):1–16, 2019.

[71] M Norouzi, S Dorrani, H Shokri, and O Anwar Bég. Effects of viscous dissipation on miscible thermo-viscous fingering instability in porous media. *International Journal of Heat and Mass Transfer*, 129:212–223, 2019.

[72] Manojkumar Gudala and Suresh Kumar Govindarajan. Numerical modelling of coupled single-phase fluid flow and geomechanics in a fractured porous media. *Journal of Petroleum Science and Engineering*, 191:107215, 2020.

[73] Manojkumar Gudala and Suresh Kumar Govindarajan. Numerical modeling of coupled fluid flow and geomechanical stresses in a petroleum reservoir. *Journal of Energy Resources Technology*, 142(6):063006, 2020.

[74] Manojkumar Gudala and Suresh Kumar Govindarajan. Numerical investigations on two-phase fluid flow in a fractured porous medium fully coupled with geomechanics. *Journal of Petroleum Science and Engineering*, 199(December 2020):108328, 2021. ISSN 09204105. doi: 10.1016/j.petrol.2020.108328. URL `https://doi.org/10.1016/j.petrol.2020.108328`.

[75] Gavin J Bowden, Graeme C Dandy, and Holger R Maier. Input determination for neural network models in water resources applications. part 1—background and methodology. *Journal of Hydrology*, 301(1-4):75–92, 2005.

[76] Gavin J Bowden, Holger R Maier, and Graeme C Dandy. Input determination for neural network models in water resources applications. part 2. case study: forecasting salinity in a river. *Journal of Hydrology*, 301(1-4):93–107, 2005.

[77] Janez Demšar, Tomaž Curk, Aleš Erjavec, Črt Gorup, Tomaž Hočevar, Mitar Milutinovič, Martin Možina, Matija Polajnar, Marko Toplak, Anže Starič, et al. Orange: data mining toolbox in python. *the Journal of machine Learning research*, 14(1):2349–2353, 2013.

[78] S Van Rijn. *Breakthrough time of a geothermal reservoir (Estimating the impact of well spacing, reservoir and operational inputs on the breakthrough time of a geothermal doublet)*. PhD thesis, 2018.

[79] A. Ghassemi and Q. Zhang. A transient fictitious stress boundary element method for porothermoelastic media. *Engineering Analysis with Boundary Elements*, 28(11): 1363–1373, 2004. ISSN 09557997. doi: 10.1016/j.enganabound.2004.05.003.

[80] Songcai Han, Yuanfang Cheng, Qi Gao, Chuanliang Yan, Zhongying Han, and Jincheng Zhang. Investigation on heat extraction characteristics in randomly fractured geothermal reservoirs considering thermo-poroelastic effects. *Energy Science and Engineering*, 7(5):1705–1726, 2019. ISSN 20500505. doi: 10.1002/ese3.386.